Tectonophysics xxx (2014) xxx–xxx

Contents lists available at ScienceDirect

Tectonophysics

journal homepage: www.elsevier.com/locate/tecto

Influence of topography and basement depth on surface rupture morphology revealed from LiDAR and field mapping, Hope Fault, New Zealand

Narges Khajavi [a,*], Mark Quigley [a], Robert Max Langridge [b]

[a] Department of Geological Sciences, University of Canterbury, New Zealand
[b] GNS Science, Lower Hutt, Wellington, New Zealand

ARTICLE INFO

Article history:
Received 17 December 2013
Received in revised form 21 May 2014
Accepted 28 May 2014
Available online xxxx

Keywords:
Hope Fault
Hurunui segment
LiDAR
Fault deformation zone
Dextral strike-slip
Topography

ABSTRACT

High-resolution airborne LiDAR and field mapping were used to investigate a 29 km-long section of the Hurunui segment of the Hope Fault concealed beneath beech forest. Approximately 20 km of the dextral strike-slip principal slip zone (PSZ) was identified as a series of 69 individual fault strands on the LiDAR DEM. Mapping revealed 70 normal, 55 dextral-reverse, and 100 secondary faults, many of which were previously unrecognized. Secondary faults are kinematically linked with the PSZ and comprise a complex surface fault deformation zone (FDZ). A Rose diagram weighted by the lengths of the PSZ strands shows that the Hurunui segment strikes between 070° and 075° and is optimally oriented for dextral strike-slip within the regional stress field. The observed fault zone complexity is thus unlikely to result from large-scale fault mis-orientation with respect to regional stresses. FDZ width measurements from 415 locations reveal a spatially-variable, active FDZ up to ~500 m wide with an average width of 200 m. FDZ width increases with increased hanging wall topography and increased topographic relief (e.g., adjacent to high topography with deeply incised streams), suggesting that along-strike topographic perturbations to fault geometry and stress states increase fault zone complexity and width. Where adjacent PSZ strands strike between 070° and 075°, the FDZ is ≤150 m wide, however, FDZ width increases where the tips of adjacent PSZ segments locally vary in strike by ≥10°. FDZ width and surface fracture density also appear to increase with increasing thickness of alluvial deposits overlying bedrock. Our results indicate that spatial variations in near-fault topography and geology can generate along-strike variability in the morphology of surface ruptures, even in the case of fast-slipping, structurally mature faults where more confined, simplistic ruptures are expected at seismogenic depths.

1. Introduction

Fault deformation zones (FDZs) typically consist of narrow (<2–5 m) principal slip zone(s) (PSZ) along which maximum fault slip occurs and a wide (>10^2 m) zone of smaller faults, fractures and/or distributed folding (e.g., Schulz and Evans, 2000; Shipton and Cowie, 2001). Field data (e.g., Joussineau and Aydin, 2009; Kim et al., 2004; Martel et al., 1988; Rockwell and Ben-Zion, 2007; Sagy et al., 2007; Stirling et al., 1996; Tchalenko and Ambraseys, 1970), numerical models (e.g., Aydin and Schultz, 1990; Richard et al., 1991), and analogue experiments (e.g., Richard, 1991; Richard et al., 1995; Riedel, 1929; Tchalenko, 1970) predict that the FDZ should narrow in width and evolve from structurally complex to simple through-going fracture patterns as strain localizes with progressive slip, although alternative models for fault zone widening with cumulative slip have been proposed (e.g., Ben-Zion and Andrews, 1998). In general, the majority of studies suggest that structurally mature active faults with large accommodated strain, fast slip rates and more frequent surface ruptures should have relatively narrow and simple rupture morphologies compared to less evolved, more segmented faults with slower slip rates. Although discrete, structurally simple rupture zones of <30 m width are common along some segments of major fast-slipping active faults (e.g., Lin et al., 2012; Sieh and Jahns, 1984; Zhou et al., 2010), rupture zones along many active faults, including evolved and fast-slipping faults in plate boundary zones, commonly exceed 10^2–10^3 m and contain complex surface rupture morphologies (Table 1). Progressive rotation and/or structural overprinting of faults misaligned with regional stresses (Scholz et al., 2010), fault zone segmentation and termination (e.g., Elliott et al., 2009; Kim et al., 2004; Oglesby, 2005; Wesnousky, 1988), and variations in the thickness and material properties of the faulted media (e.g., Barth et al., 2012; Norris and Cooper, 1997; Oskin et al., 2012; Richard et al., 1991, 1995; Shipton and Cowie, 2003) all offer explanations for the width and complexity observed in surface rupture morphology. Shallow (<1–4 km depth) stress perturbations resulting from topographic loading from mountain ranges and unloading

* Corresponding author.
E-mail address: narges.khajavi@pg.canterbury.ac.nz (N. Khajavi).

http://dx.doi.org/10.1016/j.tecto.2014.05.032
0040-1951/

Table 1
Comparison of deformation zones and slip rates of selected strike-slip faults. * includes maximum distance of distributed surface rupturing, including parallel faults, splay faults, and faults not structurally linked to principal fault, that ruptured coevally with the principal fault.

No	Dextral-slip fault/segment	Fault deformation zone width	Dextral slip rate	Reference
1	Hurunui geometric segment of the Hope Fault, *New Zealand*	~500 m	~8–13 mm/yr	This study, Langridge and Berryman (2005)
2	Conway geometric segment of the Hope Fault, *New Zealand*	~2 km	23 ± 4 mm/yr	McMorran (1991), Ward (2000), Eusden et al. (2000, 2005), Langridge et al. (2003)
3	Hope River rupture segment of the Hope Fault, *New Zealand*		~10–18 mm/yr	Freund (1971), Cowan (1989), Cowan (1990), Cowan and McGlone (1991)
	Excluding step-overs or bends	20–50 m		
	Including step-overs or bends	2.3 km		
4	Central segment of the Alpine Fault, *New Zealand*	~1 km	~28 mm/yr	Barth (2013), Norris and Cooper (2001)
5	Central segment of the Wairarapa Fault, *New Zealand*	~350 m	~12 mm/yr	Carne and Little (2012)
6	Awatere fault, *New Zealand*	~2 km	~4–7 mm/yr	Little (1996)
7	Clarence fault, *New Zealand*	~1.5 km	~4–8 mm/yr	Browne (1992), Nicol and Van Dissen (2002)
8	Previously-unidentified Greendale fault, *New Zealand*		N/A	Quigley et al. (2012)
	Excluding step-overs	~300 m		
	Including step-overs	~1 km		
9	Cholame segment of San Andreas fault/USA	~500 m	~35 mm/yr	Arrowsmith and Zielke (2009), Lienkaemper (2001)
10*	Newly-formed dextral fault in Gorny Altai/Russia	~4 km	N/A	Lunina et al. (2008)
11	Previously-unidentified Bam fault/Iran	~500 m	N/A	Binet and Bollinger (2005), Jackson et al. (2006)
12	Denali fault/Alaska	~1 km	~15 mm/yr	Schwartz et al. (2012), Hreinsdóttir et al. (2006)
13	North Coast segment of San Andreas fault/USA	~200 m	~16–24 mm/yr	Zachariasen and Prentice (2008)
14*	Coyote Creek fault, USA	~2.6 Km	~10 mm/yr	Dorsey (2002), Petersen et al. (2011)
15*	Imperial fault, Mexico–USA border	~6 km	~15–20 mm/yr	Petersen and Wesnousky (1994), Petersen et al. (2011)
16*	Superstition Hills fault and a previously unknown northeast-striking structure, USA	Up to 8.5 km	~2–6 mm/yr	Williams and Magistrale (1989), Petersen and Wesnousky (1994), Petersen et al. (2011)
17*	Previously-unrecognized Landers fault, US	~3.8 km	~0.4–0.6 mm/yr	Petersen and Wesnousky (1994), Petersen et al. (2011)
18*	Nojima fault, Japan	~4.5 km	~0.9–1 mm/yr	Murata et al. (2001), Petersen et al. (2011)
19	Duzce fault, a splay of the North Anatolian fault, Turkey	~700 m	~15 mm/yr	Pucci et al. (2008), Petersen et al. (2011)
20*	Lavic Lake and Bullion faults, USA	~6.8 km	0.2–0.6 mm/yr	Treiman et al. (2002), Petersen et al. (2011)
21*	Northern strand (five segments) of the North Anatolian fault, Turkey	~12 km	~20–23 mm/yr	Barka et al. (2002), Petersen et al. (2011)
22	Qingchuan fault of the Long Shan Thrust Belt, China	Generally <20 m Locally >100 m	~1–1.5 mm/yr for LSTB Faults	Lin et al. (2009), Lin et al. (2012)

associated with valley systems (Barth et al., 2012; Eusden et al., 2000, 2005; Norris and Cooper, 1995) may also influence surface rupture morphology. Understanding the morphology and causative mechanisms influencing surface ruptures on active faults is important for assessing future coseismic displacements and related fault rupture hazard to infrastructure adjacent to known active faults (e.g., Honegger et al., 2004; Van Dissen et al., 2013) including design of fault set-back distances (e.g., Villamor et al., 2012).

Active faults have traditionally been mapped using field techniques and aerial photography, however faults in areas of dense vegetation and/or subtle features such as small, secondary faults comprising fault zones were typically challenging to detect (Chan et al., 2007). Recently, airborne LiDAR (light detection and ranging) data has improved the detection of faults in densely vegetated areas and the resolution with which faults can be mapped (Arrowsmith and Zielke, 2009; Barth et al., 2012; Begg and Mouslopoulou, 2010; Chan et al., 2007; Duffy et al., 2013; Gold et al., 2013; Haddad et al., 2012; Langridge et al., 2013, 2014; Nissen et al., 2012; Oskin et al., 2012; Quigley et al., 2012; Zachariasen and Prentice, 2008). In this paper we use LiDAR data to map the surface rupture patterns associated with major earthquakes on the Hurunui segment of the Hope Fault in New Zealand's South Island. We map and classify the structures within the FDZ, analyse their kinematics in the context of the regional stress field, and investigate how the FDZ width and geometry vary as a function of fault orientation, topography, and depth-to-bedrock. We discuss the applicability of our new fault zone maps for characterizing fault paleoseismicity. We provide explanations for why complex surface ruptures may form on structurally mature faults where kinematically simple slip confined to a discrete rupture may have been expected.

2. Tectonic and geologic setting

New Zealand occupies the boundary between the Australian and Pacific tectonic plates. Nearly pure strike-slip deformation occurs across the Marlborough Fault System in the northern South Island at rate of 39–48 mm/yr along an azimuth of ~258° (Beavan et al., 2002; DeMets et al., 1994, 2010; Wallace et al., 2007, 2012) (Fig. 1). The Marlborough Fault System is characterized by four major dextral strike-slip faults (Wairau, Awatere, Clarence, and Hope faults) that transfer the motion between the Alpine Fault in the west and Hikurangi subduction zone in the east (Berryman and Beanland, 1991; Pettinga et al., 2001; Van Dissen and Yeats, 1991; Wallace et al., 2007, 2012; Yeats and Berryman, 1987) (Fig. 1). The Wairau, Awatere and Clarence faults have Quaternary slip rates of ~4–8 mm/yr (Benson et al., 2001; Berryman et al., 1992; Knuepfer, 1992; Little and Jones, 1998; Nicol et al., 2002; Zachariasen et al., 2006). The ENE-striking and NW-dipping Hope Fault is a ~230 km dextral strike-slip fault that traverses the central South Island of New Zealand from the Alpine Fault in Westland to the east coast of the South Island near Kaikoura (Fig. 1) (Cowan, 1990; Freund, 1971; Langridge and Berryman, 2005; Langridge et al., 2003; Van Dissen, 1989). The Hope Fault has the highest slip rate of 23 ± 4 mm/yr (Langridge et al., 2003) within the Marlborough Fault System.

The bedrock geology of the Marlborough region consists primarily of sandstones, mudstones and mélange collectively classified as the Torlesse Formation of Triassic to early Cretaceous age (Barrell and Townsend, 2012; Gregg, 1964; Nathan et al., 2002; Warren, 1967). The basement rock is covered with late Quaternary unconsolidated deposits (Barrell and Townsend, 2012) as Tertiary rocks were eroded away. Within the study area, the late Quaternary period is characterized by ice cap and valley glaciers, the latter being the dominant force in forming the Hurunui and Hope valleys (Nathan et al., 2002) (Fig. 2). During cold climate periods, glacial ice eroded the mountainous areas while glacial meltwater deposited volumes of sediments in the valleys and basins. Following the Last Glacial Maximum (LGM-Otira glaciation; about 12,000 years ago) (Nathan et al., 2002), alluvial aggradation terraces and fans were formed and slopes were stabilized by growth of woody vegetation. Subsequent to this, rivers incised into these surfaces (Barrell and Townsend, 2012; Knuepfer, 1992). Glaciofluvial, alluvial and landslide/debris deposits of late Pleistocene to Holocene age thus predominate in valleys and basins across which the Hope

Please cite this article as: Khajavi, N., et al., Influence of topography and basement depth on surface rupture morphology revealed from LiDAR and field mapping, Hope Fault, New Zealand, Tectonophysics (2014), http://dx.doi.org/10.1016/j.tecto.2014.05.032

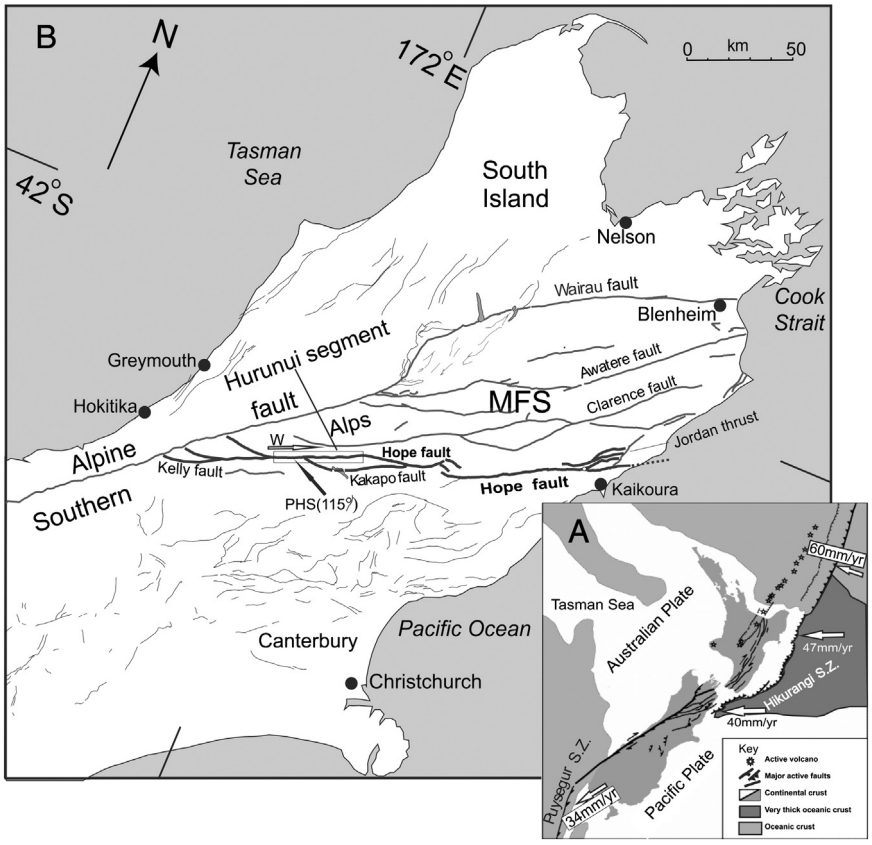

Fig. 1. Geological setting of New Zealand and active faults in the northern South Island. (A) New Zealand plate boundary including subduction zones and major faults. Nuvel-1 plate rates (mm/yr) and orientations are after DeMets et al. (1994). (B) Location of active faults within the northern South Island. Marlborough Fault System (MFS) and the Alpine Fault are highlighted. Hope Fault is heavily highlighted with the Hurunui segment shown in a rectangle; modified from Langridge and Berryman (2005). The principal horizontal shortening vector (PHS, Nicol and Wise, 1992; Pettinga and Wise, 1994), and the modelled relative slip vector (W; Wallace et al., 2007, 2012) are shown near the Hurunui segment.

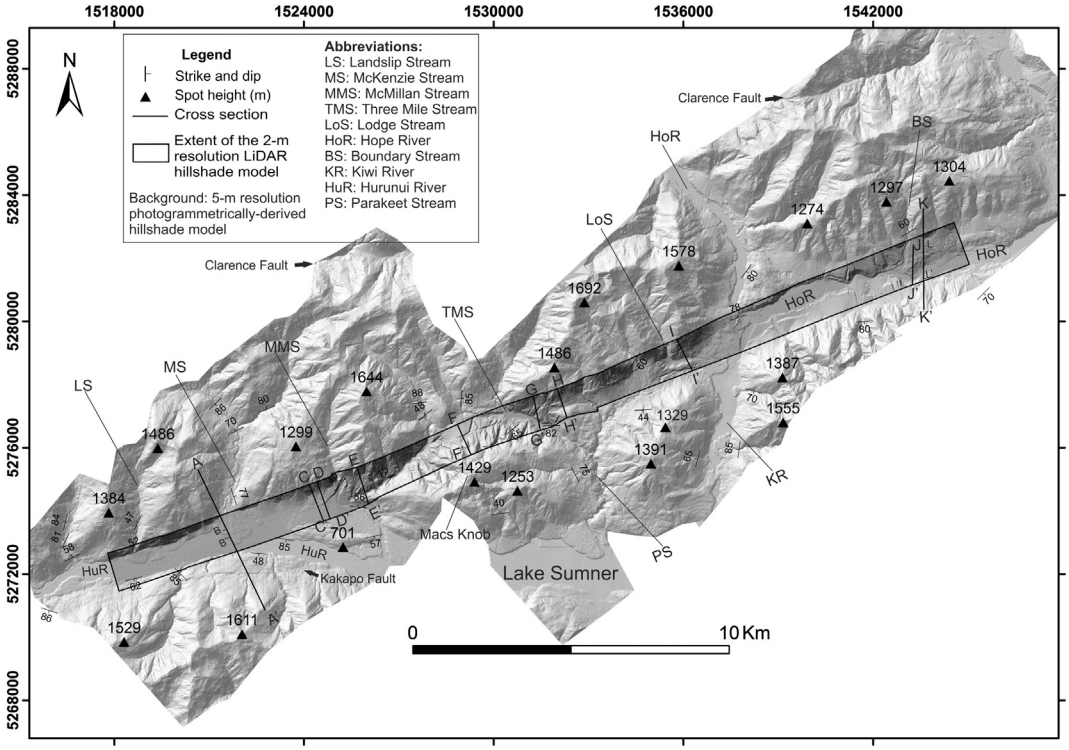

Fig. 2. Geomorphic location of the LiDAR strip. Base map, which is our photogrammetrically-derived 5-m hillshade model, is used to give a larger view of the landscape.

Please cite this article as: Khajavi, N., et al., Influence of topography and basement depth on surface rupture morphology revealed from LiDAR and field mapping, Hope Fault, New Zealand, Tectonophysics (2014), http://dx.doi.org/10.1016/j.tecto.2014.05.032

Fault traverses (Nathan et al., 2002). In such a dynamically active landscape, the geomorphic features created are the result of interaction between erosion, deposition and the fast-slipping Hope Fault.

The Hope Fault is the southernmost and youngest major fault within the Marlborough Fault System, and likely initiated ~1–2 Ma ago (Langridge and Berryman, 2005; Wood et al., 1994). The fault consists of several geometric segments and some branching faults (Berryman et al., 2003; Langridge et al., 2003, 2013; Pettinga et al., 2001; Van Dissen and Yeats, 1991; Yang, 1991) (Fig. 1). Along the Hope Fault, many geomorphic features preserve dextral, vertical, or oblique displacements resulting from past earthquakes.

The eastern segments of the Hope Fault are more easily mapped (Eusden et al., 2000, 2005; Beauprêtre et al., 2012) due to drier, less forested landscape and anthropogenic activity that has resulted in a largely grass-covered environment (Langridge et al., 2014). A FDZ width of up to 1.3 km including depressions, folds, and wedges has been documented along the eastern parts of the Hope Fault where it is not concealed beneath forest (Cowan, 1989; Eusden et al., 2000, 2005; Freund, 1971). Fault dip angles of 59°–80° NW measured from bedrock exposures have been published for the eastern segments of the Hope Fault (Eusden et al., 2000, 2005; Freund, 1971).

This study focuses on the Hurunui segment of the Hope Fault, which is a 42-km-long geometric segment located between Harper Pass in the west and the Hope-Boyle River confluence in the east (Figs. 1 and 2) (Cowan, 1991; Langridge and Berryman, 2005; Langridge et al., 2013). The Hurunui segment is located east of the main divide of the Southern Alps, where average annual rainfall is ~1.5–3 m (Langridge et al., 2014). Here, much of the landscape is covered by native beech forest (Langridge and Berryman, 2005; Langridge et al., 2013, 2014). The record of large earthquakes on the Hurunui segment is uncertain due to the short historical period (from ca. A.D. 1840) (Langridge et al., 2013) and remote mountainous location of this segment. Documentation of the surface rupture attributes of the fault is thus required to better estimate the fault slip rate and paleoseismic attributes such as magnitude and recurrence interval. Along this segment, major fault strands and scarps, near-fault geomorphic features such as grabens, fissures, sag ponds, and dextrally and vertically offset geomorphic markers such as terrace risers and streams have been documented by Langridge (2004), Langridge and Berryman (2005), and Langridge et al. (2007, 2013). Much of their mapping was undertaken in forested terrain using traditional methods and through re-interpretation of aerial images initially used by Freund (1971) to map the fault. The location of the PSZ and major structures within the FDZ was previously identified on regional geologic maps (Bowen, 1964; Gregg, 1964; Lensen, 1962; Nathan et al., 2002; Rattenbury et al., 2006; Warren, 1967). Dextral displacements along the fault yield a dextral to vertical slip ratio of ~7 ± 2:1 (Langridge and Berryman, 2005), indicating that the fault is predominately strike-slip and likely to be steeply dipping. Bedrock fault exposures show that the Hurunui segment dips steeply to the northwest (strike/dip = 063°/80° NW; Langridge and Berryman, 2005) in a bedrock shear zone near Three Mile Stream (Fig. 2) and in an outcrop of intense crushed bedrock including the fault plane (088°/72° NW; Browne, 1987) east of the study area (off the LiDAR swath). Langridge and Berryman (2005) estimated two dextral slip rates for the Hurunui segment; 8.1–11 mm/yr for the McKenzie fan site, and 13 ± 1.5 mm/yr for the Macs Knob area (Fig. 2). Estimates of the Hurunui segment surface rupture length (42 km), average single event displacement (3.4 m) and seismogenic depth (13 km) applied to earthquake scaling relationships (Hanks and Kanamori, 1979; Langridge and Berryman, 2005; Stirling et al., 2002, 2008; Wells and Coppersmith, 1994) yield M_w estimates of 7–7.4 (see also Langridge and Berryman, 2005).

In this study, airborne LiDAR data was collected along a 29-km-long and ~1-km wide survey along the centremost part of the Hurunui segment (Langridge et al., 2014). This survey extends from Landslip Stream in the west to near Boundary Stream in the east (Fig. 2). In particular, the survey was designed to assess the potential of LiDAR beneath beech (*Nothofagus*) forest in an area that was previously mapped by Langridge (2004), Langridge and Berryman (2005), and Langridge et al. (2007, 2013).

3. LiDAR data

Airborne LiDAR data and orthophotos were collected along the Hurunui segment in November 2010. The data were acquired with an Optech ALTM 3100EA instrument from a plane at the flight altitude of ~1200 m above ground level (Langridge et al., 2014). For grassland and gravel substrates, the number of ground returns was approximately equal to the signal input; i.e., ~100%. For the forested terrain, up to 3–4 times the number of total returns were counted (Langridge et al., 2014). Unclassified returns collected from the vegetated terrain and were filtered in-house by New Zealand Aerial Mapping Ltd. (NZAM) (Langridge et al., 2014) and automatically classified into ground, first and intermediate returns using TerraSolid LiDAR processing software modules TerraScan, TerraPhoto and TerraModeler. Manual editing was subsequently used to improve the quality of the classified ground control points. Ground return point data for sample areas of gravel, grassland, scrub and beech forest were 1.47, 1.60, 0.78, and 0.7 points/m^2 respectively (Langridge et al., 2014). Horizontal and vertical accuracy of LiDAR data points are ±0.3 m and ±0.15 m respectively. Ground return point data was used to construct high resolution 2 m DEM and 0.5 m contour lines.

To generate the DEMs and hillshade models for mapping, we used ASCII xyz data from the ground returns and produced feature classes using ArcMap (GIS) software. An inverse distance weighted (IDW) interpolation technique was utilized to build the DEMs. In this method, input parameters of number of points = 12 and maximum distance = 20 were used based on the visible gaps in our dataset. Fig. 2 shows the extent of the LiDAR-derived 2 m hillshade model that overlaps our photogrammetrically-derived 5 m hillshade model. Socet GXP software (http://www.geospatialexploitationproducts.com/content/products/socet-gxp) and 2008 aerial images were used to extract the 5 m DEM. The high resolution 5 m hillshade model was used as a background to show geomorphic context of the study area. The 2 m DEM and hillshade models were used to map the fault and geomorphic features. Along with the LiDAR DEM and hillshade models, complementary digitized files such as topographic maps, pre-LiDAR 15 m DEM, our 5 m hillshade model, geological maps (Nathan et al., 2002; Rattenbury et al., 2006), and orthophotos were imported into ArcMap software and a suite of discrete shapefiles were developed to map tectonic and geomorphic features.

4. Methodology

4.1. Geomorphic mapping

To generate a detailed geomorphic map of the study area, we used all of the complementary maps, examined elevation profiles on the 2 m DEM, used multiple illumination angles in shade models in ArcMap, and field-validated the results. Geomorphically active and abandoned vegetated alluvial fans, active and ephemeral rivers, terraces risers, vegetated (older) and unconsolidated (younger) landslides/debris deposits, active flood plains, swamps, ponds, talus/scree slopes, gravitational failure scarps (arcuate features), cut banks/cliffs, moraine (with less certainty), and tectonic features such as grabens, fold axes, and pop-up (bulge) structures were mapped.

4.2. Fault mapping and classification

GIS-based mapping was integrated with our field checking and previous field studies to identify all fault strands. Following that a classification of the faults based on kinematics, orientation, and spatial distribution with respect to the Hope Fault was required. Generally, FDZs

Please cite this article as: Khajavi, N., et al., Influence of topography and basement depth on surface rupture morphology revealed from LiDAR and field mapping, Hope Fault, New Zealand, Tectonophysics (2014), http://dx.doi.org/10.1016/j.tecto.2014.05.032

consist of a PSZ and three other main zones; tip damage zone (at tips of the PSZ), linking damage zone (at step-overs), and wall damage zone (around the PSZ) (Kim et al., 2004). There are defined structures that mark each zone that have been well-described in dextral strike-slip fault systems in the field and laboratory experiments (Kim et al., 2004; Richard et al., 1991, 1995; Riedel, 1929; Scholz, 1977; Sylvester, 1988; Tchalenko, 1970; Tchalenko and Ambraseys, 1970). We produced a simple sketch map to show these structures and to provide a foundation for our fault classification (Fig. 3).

Fig. 3A shows a schematic configuration of structures associated with dextral strike-slip systems. Riedel (R) faults (synthetic strike-slip faults), R′ faults (antithetic strike-slip faults; conjugate R), P faults (synthetic minor faults), P′ faults (antithetic minor faults; conjugate P), Y faults (synthetic strike-slip faults subparallel to the PSZ) and T faults (synthetic micro faults subparallel to the PSZ; also called tension gashes or extension fractures) that initiate when shearing begins (Carne and Little, 2012; Casas et al., 2001; Kim et al., 2004; Richard et al., 1995; Scholz, 1977; Sylvester, 1988; Tchalenko, 1970). As shear continues, normal (N) and reverse (Re) faults also form and will be rotated by ongoing shear. All of these structures may be superimposed depending on the natural stress conditions and material properties of the faulted substrate, resulting in a structurally complex fault zone (Burbank and Anderson, 2006). These faults are mainly part of the wall damage zones. Splay faults (Sp) are branch faults that are dominant in the tip damage zones, and can mainly be in the form of wing cracks, horsetail splays (pinnate fractures), synthetic, and antithetic faults, but sometimes combinations of these forms occur (Kim et al., 2004). In contrast, Fig. 3B shows a schematic configuration of the structures that we mapped on the LiDAR swath along the Hurunui segment. Here, we generally categorize the structures into three groups; 1) continuous fault strands that define the PSZ, 2) fault strands that are near the PSZ and connect to the PSZ on the surface, and 3) fault strands that are within the FDZ, but are farther away from the PSZ and have no directly observable physical connection to it on the surface. We name the third group "secondary faults" (Sf).

The first group is composed of the PSZ, and inferred PSZ strands. We discriminate the PSZ strands from other faults confidently because they display well-developed surface expression and fault scarps, appear continuous and traceable, and accommodate considerable cumulative dextral and vertical slip measurable along offset geomorphic landmarks. The inferred PSZ strands are those with lesser confidence, but are parallel to, and located along, surface projections of adjacent PSZ strands and thus are likely of similar origin. This group includes continuous short or long strands, or continuous en echelon faults (Fig. 3B).

The second group is composed of normal (N), dextral-reverse (Re) and splay (Sp) faults, and some lineaments (L) with no discernible offset. We do not observe an abundance of R shears along the LiDAR swath. This is possibly because erosional or depositional processes have obscured or removed evidence for previous strike-slip displacements more readily than structures with vertical displacement, or that these structures are not a primary feature of coseismic rupture here. The kinematics and orientation of these structures with respect to the PSZ were used to determine whether they are normal, dextral-reverse, splay, or R faults. Kinematic information was obtained from vertical and horizontal displacements of streams, terrace risers, bulges or basins. Orientations of delineated structures (Fig. 3B) were compared with orientations of classically defined structures (Fig. 3A) with respect to the PSZ. Both the orientation and offsets observed across N, Re and Sp faults indicate that some of these structures include strike-slip components of displacement, and may in some cases be dominated by strike-slip movement where structures are close in orientation to the PSZ. We extended numerous elevation profiles across every structure to

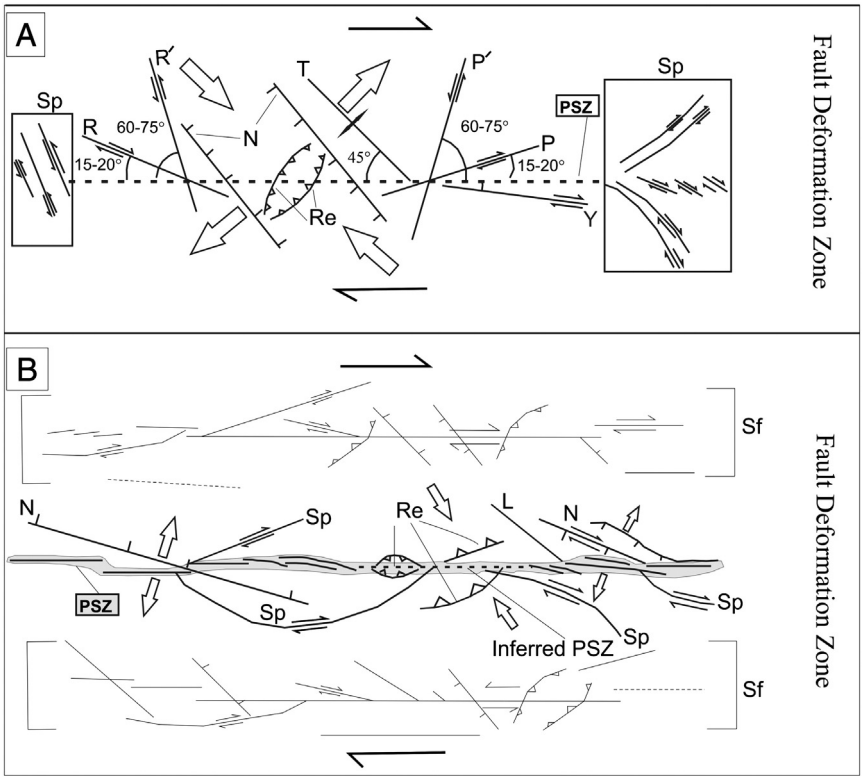

Fig. 3. Recorded structures associated with strike-slip system are compared with structures associated with the dextral strike-slip Hurunui segment of the Hope Fault using a simplified sketch map. (A) Structures form in models and natural settings (after Tchalenko, 1970; Scholz, 1977; Sylvester, 1988; Richard et al., 1995; Casas et al., 2001; Kim et al., 2004; Carne and Little, 2012). (B) Structures identified on the LiDAR strip. Abbreviations were explained in detail within the text.

Please cite this article as: Khajavi, N., et al., Influence of topography and basement depth on surface rupture morphology revealed from LiDAR and field mapping, Hope Fault, New Zealand, Tectonophysics (2014), http://dx.doi.org/10.1016/j.tecto.2014.05.032

examine their kinematics and geomorphology more carefully, and field-assessed many of them to improve confidence in our classifications.

The third group (Sf) is composed of many fault strands that characterize the boundary of the FDZ. These faults are accommodated in the hanging wall (HW) and foot wall (FW) blocks around the PSZ, in a distance of up to 350 m on the steep slopes, and quite often show asymmetric patterns with respect to the PSZ. At some localities along the FDZ, these faults appear in the form of a smaller-scale dextral strike-slip system which includes its own PSZ and related structures (Fig. 3B). Since secondary faults display smaller vertical and horizontal displacements along their length, they cannot be mistakenly considered as being the PSZ or the core of the FDZ.

4.3. Relationships between fault orientation, kinematics and FDZ width

For kinematic analysis, strikes and lengths of the PSZ and inferred PSZ strands, normal, and dextral-reverse faults were measured on the LiDAR strip. To provide significant azimuthal distribution of the faults in each group (Azzaro et al., 2012; Barth et al., 2012), we weighted the strikes of the faults based on their lengths and present them on Rose diagrams in Fig. 4.

For analysis of the FDZ, we measured the widths of the FDZ, including all of the mapped structures on the LiDAR DEM, along the entire length of the survey (Fig. 5). We made 330 measurements of the FDZ width along the fault length, with an average spacing of 80 m between measurements. Where the FDZ width was highly variable along the PSZ, we increased the number of the measurements to 10 m spacing. Where the FDZ is uniformly narrow (<10 m) along strike and limited to the delineated fault scarp, we decreased the spacing of measurements to 1 km. A detailed graph showing the variations of the FDZ width along the Hurunui segment is presented in Fig. 5. To show the spatial distribution of the FDZ width on the HW and FW blocks, we used a similar methodology as described above except that we made 415 measurements of the FDZ width north and south of the PSZ. We designated positive signs to the values of the FDZ width measured north of the PSZ, and negative signs to the values of the FDZ width measured south of the PSZ to assess the symmetry of the FDZ with respect to the PSZ along the Hurunui segment (Fig. 6).

For evaluating the effect of fault strike on width of the FDZ, we plotted the strikes of the PSZ strands along the fault length. The plot was then overlain on the graph that shows the variations of the FDZ width along the fault (black closed circles on Fig. 5). To assess if the local variations in strikes of the PSZ strands can influence the FDZ width or its spatial distribution, we considered the difference between strikes of the adjacent PSZ strands and plotted the differential values as a bar graph along the fault length (red bars on Fig. 6).

4.4. Relationships between topography and FDZ width

For evaluating the effect of topography on the FDZ width, we extended two PSZ-parallel topographic profiles, with the same length, on the 2 m LiDAR DEM at 300 m distance north and south of the PSZ. Each profile is used to represent the average near-field topography south or north of the fault. To avoid confusion by adding these two topographic profiles, we made a differential topographic profile and overlaid it on Fig. 6 (DT1; red profile). This differential profile is the result of subtracting the southern profile from the northern one. Therefore, where this profile shows values >0, north of the fault is higher in elevation than south of it, where it shows values <0, south of the fault is higher in elevation than north of it, and where there is no difference in the elevation of north and south of the fault, the profile shows zero (0) values. Additionally, we extended 4 other PSZ-parallel topographic profiles; two of which were produced from our photogrammetrically-derived 5 m DEM at 1 km distance north and south of the PSZ, and two others on the 15 m DEM at 1.5 km distance north and south of the PSZ. Using a similar methodology to that described above, we made 2 more differential profiles and overlaid them on Fig. 6 (DT2; the green profile and DT3; the orange profile). The reason for adding extra profiles is that they represent the farther-field topography of south and north of the PSZ. The 5 m DEM had much better resolution for extracting distal elevation profiles, but its width was variable along the PSZ forcing us to use the 15 m DEM for the distal profiles. We also extracted the on-fault topography from the LiDAR DEM and added it to Fig. 6 to show the elevation of the landscape cut by the fault. By overlaying the differential profiles on Fig. 6, we can qualitatively assess the

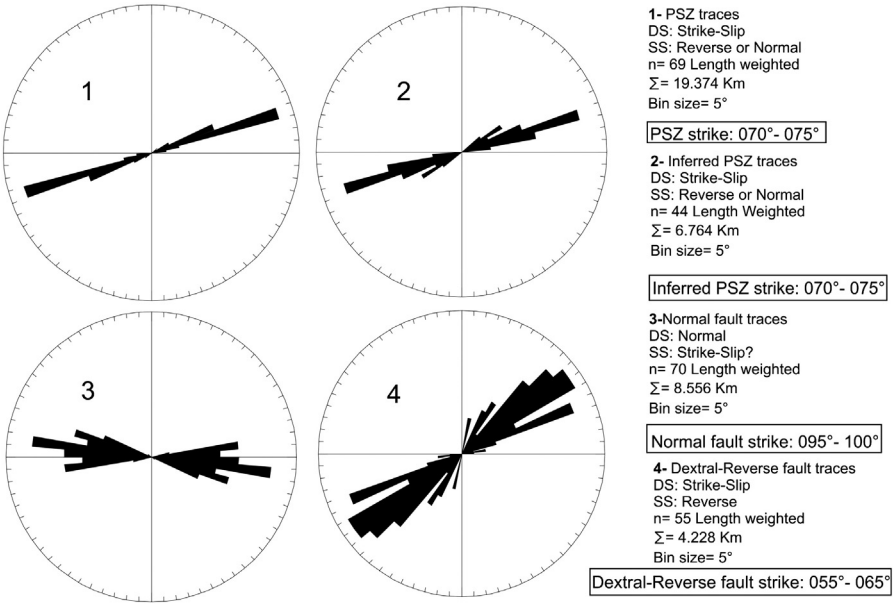

Fig. 4. Rose diagrams showing the significant azimuthal distribution of the PSZ and inferred PSZ strands, normal and dextral-reverse faults mapped along the Hurunui segment. Details of each group of faults are provided. Abbreviations: DS; Dominant sense of motion, SS; Subordinate sense of motion.

Please cite this article as: Khajavi, N., et al., Influence of topography and basement depth on surface rupture morphology revealed from LiDAR and field mapping, Hope Fault, New Zealand, Tectonophysics (2014), http://dx.doi.org/10.1016/j.tecto.2014.05.032

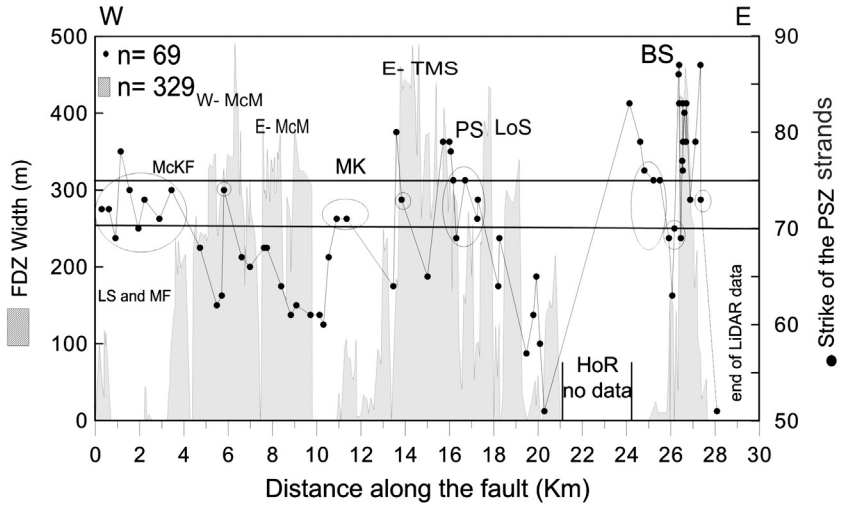

Fig. 5. Width of the FDZ with respect to the PSZ, strike of the PSZ strands, and the range of significant azimuthal distribution of the PSZ (right axis) are shown along the fault. Width of the FDZ is defined using the location of the structures off the PSZ. Abbreviations: LS and MF: Landslip Stream and Matagouri Flat, McKF: McKenzie Fan, W-McM: West McMillan, E-McM: East McMillan, MK: Macs Knob, E-TMS: East Three Mile Stream, PS: Parakeet Stream, LoS: Lodge Stream, HoR: Hope River, BS: Boundary Stream.

spatial relationships between topography adjacent to the fault and the width of the FDZ.

4.5. Structure contours of PSZ strand to constraint near-surface fault dip

Structural contours were constructed along the length of the PSZ to provide estimates of near-surface fault dip. We estimated the fault dip from three locations; east of McMillan Stream (distance 7.5–9 km on Figs. 2 and 5), Macs Knob (distance 10–13.5 km on Figs. 2 and 5), and Lodge Stream (distance 18–20 km on Figs. 2 and 5). Measurements of near-surface dip were then compared with nearby measurements of bedrock fault zones or fractures (e.g., Langridge, 2004) to estimate fault subsurface geometries through the cover and into the bedrock (see Section 4.6).

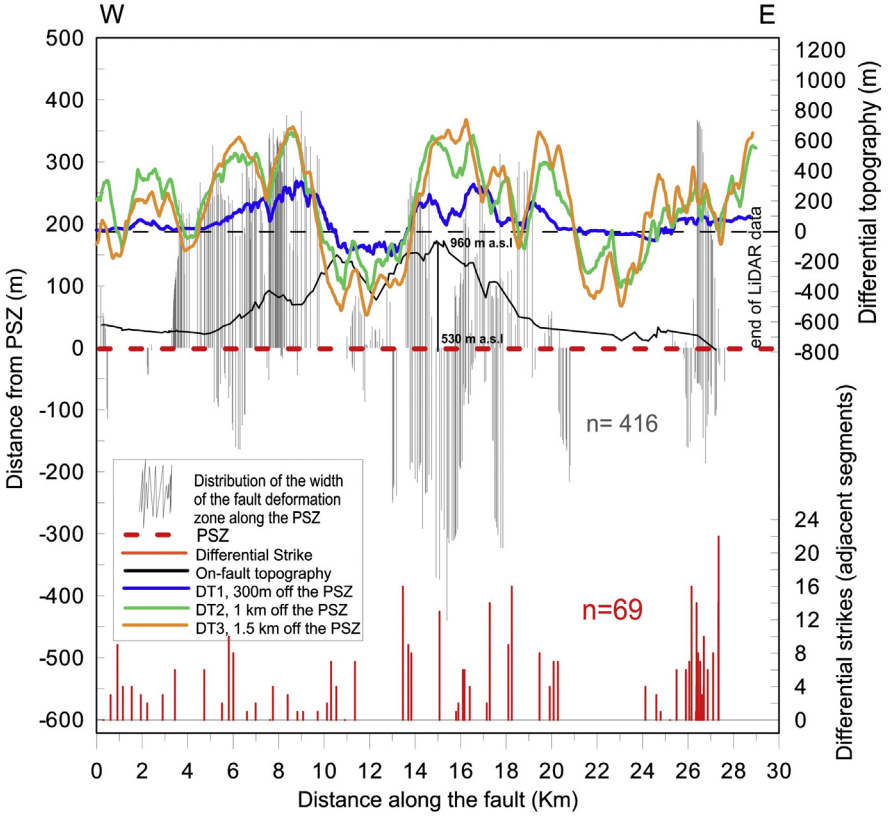

Fig. 6. Detailed analysis of the FDZ associated with the Hurunui segment of the Hope Fault. Width of the FDZ is defined using the location of the structures off the PSZ. Changes in strike of the adjacent fault strands (i.e., differential strike which reflects step-overs or bends) and differential topography were examined against each other. Northern (positive values) and southern (negative values) portions of the FDZ with respect to the PSZ (grey bar graph), differential topographic profiles (DT1-3), on-fault topographic profile, and differential strikes (red bar graph) are shown.

Please cite this article as: Khajavi, N., et al., Influence of topography and basement depth on surface rupture morphology revealed from LiDAR and field mapping, Hope Fault, New Zealand, Tectonophysics (2014), http://dx.doi.org/10.1016/j.tecto.2014.05.032

4.6. Relationships between depth-to-basement and FDZ width

For evaluating the effect of sediment thickness (overlying bedrock) on FDZ width, we first selected sites along the LiDAR swath to construct cross-sections. Three characteristics were considered in sample site selection; 1) the existence of abundant or complex structures, 2) the appearance of different styles of faulting such as N-facing vs. S-facing scarps, and en echelon vs. confined PSZ traces, and 3) areal coverage of different parts of the landscape, i.e., young, active alluvial valleys cut by the fault versus active mountain fronts cut by the fault. The sites, from west to east, are McKenzie fan, east and west of McMillan Stream, Macs Knob, and east of Three Mile, Lodge, and Boundary Streams (Fig. 2).

To generate accurate profiles and structural cross-sections of the sample sites, we used both the 2 m LiDAR and the 5 m DEMs as basemaps depending on the extent of the profiles. Cross-sections AA′ to LL′ were extended across the PSZ through the selected sites (Fig. 2). Exposed bedrock slopes (BS) were uniformly extrapolated down to the base of the profiles assuming constant dip to estimate the depth-to-bedrock along the cross-section. We have no direct constraints on the depth and shape of the bedrock interface beneath alluvial deposits, thus this is an extrapolated model only. The hypothesized geometry of the cover deposits beneath the FDZ is used to calculate the average depth-to-bedrock. For example; where geometry of cover deposits is a simple triangle (cross-sections CC′, EE′, HH′ II′), the average bedrock depth will be two thirds of the triangle height, but where cover geometry is complex we split it into several simpler shapes and calculate average depth to bedrock. For cross-section EE′, where up-slope portions of the FDZ are in the bedrock, the cross-sectional areas of the sediment wedges (beneath lower-slope portions of the FDZ) were converted to a rectangular area with uniform depth and the average depth-to-bedrock beneath the FDZ width was computed using this area and the FDZ width. We also added the orientation of bedding to some of the cross-sections where strike and dip data were available (see Fig. 2, strikes and dips from Nathan et al., 2002; Langridge, 2004; Rattenbury et al., 2006). The dip angle of the fault in the near surface was estimated using structure contours (see Section 4.5) and was also constrained at two sites in excavated trenches near Boundary Stream (BS), and west of the McKenzie fan in the flood plain of the Hurunui River (Fig. 2), where the fault dip is vertical (Langridge et al., 2013; Khajavi et al., in preparation). In our cross-sections, we use a uniform dip of the fault in bedrock of 85° NW for the PSZ, dextral Sf, and dextral Sp structures in bedrock between distances 0 to 10 km and 14 to 30 km on Fig. 5 as indicated from bedrock fault exposures and the trenches east and west of the study area, and 80° SE between distances 10 to 14 km on Fig. 5, analogous to structures exposed elsewhere on other segments of the Hope Fault (e.g., Cowan, 1989; Eusden et al., 2000, 2005). For N faults we use a dip of 60° and for Re faults we use a dip of 45°; consistent with shallow structures that merge with the PSZ in the cover sequence or near the bedrock-cover interface. Using these cross-sectional models we were able to examine the influence of bedrock depth on the FDZ width and on the ratio of the number of faults/fractures to the FDZ width. The average depth-to-bedrock beneath the FDZ is plotted against FDZ width in Fig. 13A.

5. Results

A detailed structural geomorphic map was produced for the LiDAR strip (Figs. 7–10; see also the supplementary Kmz file). These figures show continuous uninterpreted LiDAR hillshade model strips (from west to east), that include sample sites (selected windows on the strips; A and B), and the equivalent geomorphic-structural maps of the sites so that uninterpreted and interpreted datasets can be visually compared.

5.1. Fault lengths and orientations

Fault mapping and classification reveal that the total length of the PSZ identifiable on the LiDAR swath is ~20 km (69% of the entire swath). The PSZ consists of 69 fault strands. The length of these fault strands expressed as tip-to-tip measurements of continuous rupture strands varies from 30 to 1500 m. Nine PSZ strands are longer than 500 m and 3 are longer than 1 km. The mean length of the PSZ strands is 280 m. The total combined length of the inferred PSZ strands (not visible on LiDAR but able to be linearly traced between adjacent mapped strands; shown as dashed lines) is ~7 km (24% of the entire swath). The remaining 7% of the total length of the Hurunui segment is not identifiable on the LiDAR swath and is inferred to have been eroded away or buried by active alluvial and colluvial processes (Figs. 2 and 5–6). PSZ step-over widths were measured perpendicular to the PSZ strike at 8 locations where adjacent PSZ lengths were greater than 300 m; widths ranged from 17 to 90 m (average = 58 m).

In addition to the PSZ and inferred PSZ strands, 70 normal faults and 55 dextral-reverse faults, with total lengths of 8.5 km and 4.2 km were mapped respectively. Normal faults are more abundant north of the PSZ and dextral-reverse faults are typically more abundant south of the PSZ. Many secondary (n = 100) and splay (n = 13) faults of different scale and style of motion were also mapped. Secondary faults have higher distribution north of the fault and appear mainly parallel to sub-parallel to the PSZ, however, splay faults are almost of the same size and appear near the small-scale step-overs or near the tips of the PSZ or inferred PSZ strands (Figs. 7–10).

Length-weighted Rose diagrams (Fig. 4) indicate that the longest segments of the PSZ and inferred PSZ are those with strikes of 070° to 075°, the longest segments of the normal faults are those with strikes of 095° to 100°, and the longest segments of the dextral-reverse faults are those with strikes of 055° to 065°. Disregarding the effect of weighting, the PSZ strike varies from 070° to 075°, the inferred PSZ strike varies from 065° to 075°, the normal fault strike varies from 090° to 100°, and the dextral-reverse fault strike varies from 045° to 050°. The result of the strike analysis shows that normal fault strands are oriented at an angle of 20°–30° (average 25°) clockwise with respect to the PSZ. Dextral-reverse fault strands are oriented at an angle of 5°–20° (average 12.5°) counter-clockwise with respect to the PSZ.

5.2. FDZ width and asymmetry

The results reveal that the FDZ width is spatially variable along the fault length with three major peaks (Figs. 5–6). The FDZ width varies from a few metres, where it is equivalent to the PSZ width, to up to 500 m including the three fault groups described in the methodology section (Fig. 5). The average width of the FDZ is ~200 m. The results of the FDZ width measurements with respect to the PSZ are presented in Table 2 and Fig. 6. In total, 57% of the measurements were taken north of PSZ and 33% were taken south of the PSZ (Table 2). The remainder of measurements (10%) was centrally distributed with respect to the PSZ (Figs. 5–6, Table 2). At locations where landforms of equivalent age enabled structures to be compared to the north and south of the PSZ (Fig. 6) there is considerable spatial variability in terms of the degree of symmetry about the PSZ. For instance, at distances ~5–8 km and ~26–28 km (Fig. 6), the FDZ is wider north of the PSZ than south of it, whereas at distance ~14.5–16 km (Fig. 6) the FDZ is wider to the south of the PSZ. Over much of the strike length, the FDZ as currently expressed in the landscape is highly asymmetric with respect to the PSZ. Similar asymmetry is commonly observed in exhumed strike-slip fault zones (e.g., Schulz and Evans, 2000).

Only 30% of the FDZ width north of the fault is narrower than 100 m, 55% of it is wider than 200 m and narrower than 300 m, and 15% of it is wider than 300 m (Table 2). In contrast, 48% of the FDZ width south of the fault is narrower than 100 m, 43% of it is wider than 200 m and narrower than 300 m, and only 9% of it is wider than 300 m (Table 2).

Please cite this article as: Khajavi, N., et al., Influence of topography and basement depth on surface rupture morphology revealed from LiDAR and field mapping, Hope Fault, New Zealand, Tectonophysics (2014), http://dx.doi.org/10.1016/j.tecto.2014.05.032

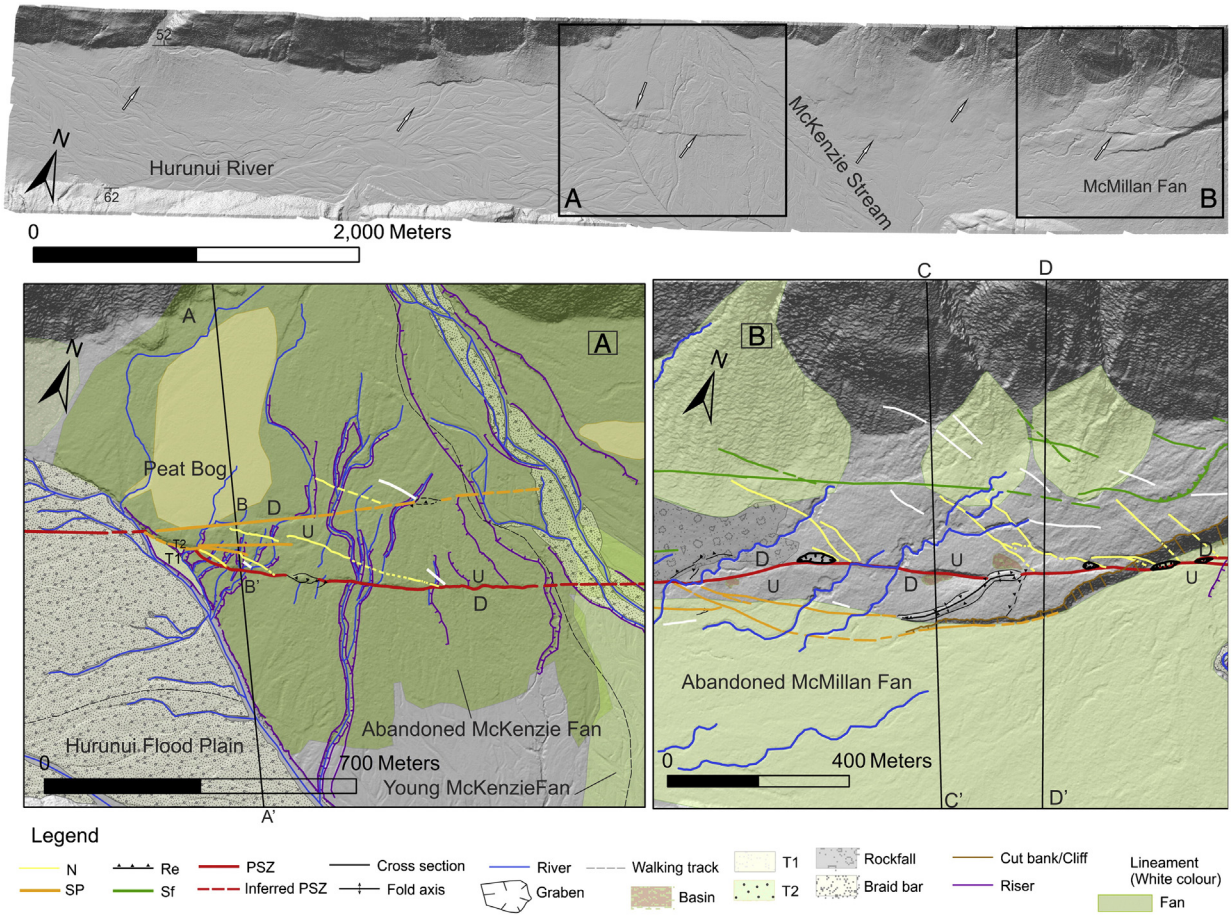

Fig. 7. Uninterpreted LiDAR strip (~7 km long, from Landslip Stream to McMillan Stream) and structural geomorphic map of the two key sites. Arrows point to the fault strands. (A) McKenzie fan and locations of cross-sections AA′ and BB′. (B) West of McMillan Stream and locations of cross-sections CC′ and DD′.

The FDZ is distributed more to the north of the PSZ, and is on average wider there, compared to the FDZ on the south side of the PSZ.

5.3. Relationship between FDZ width and PSZ orientation

Where strikes of the PSZ strands are in the range of 070°–075° the FDZ width is typically a few metres to ~200 m wide (Fig. 5). In contrast, where strikes of the PSZ strands deflect away from 070° to 075°, the FDZ width is wider and increases up to ~500 m. Differential strikes graph shows three major peaks along the fault length that are fairly concordant with wider distribution of the FDZ (Fig. 6). Differential strikes vary from 0° to 22° with an increasing trend from west to east of the LiDAR swath. The maximum local changes in strike are up to 10° in the west, 16° near the middle, and 22° toward the eastern end of the study area (Fig. 6).

5.4. Relationship between FDZ width and topography

The fault occupies open valleys and rangefronts and cuts across topography at elevations ranging from 530 to 960 m a.s.l. (Fig. 6). The results of evaluating the effect of varying topography on the FDZ width reveal that the narrowest parts of the FDZ are located where it crosses both the lowest elevation and youngest deposits (near Landslip Stream, at McKenzie fan, and near Hope Shelter) and the highest elevation and oldest alluvial fan deposits (at Macs Knob and west of Hope-Kiwi River confluence) in the study area (Figs. 2 and 5–6) indicating that the FDZ width shows no systematic relationship with landscape age or elevation. Where steep (≥25° slope) HW (north of the fault) topographic relief is present and exceeds FW relief near river valleys, secondary faults are abundant and the FDZ width is ~300–450 m (Figs. 8A and 9A–B, cross-sections GG′ and II′, and Fig. 10, cross-section JJ′). Under the same topographic configuration but farther away from the river valleys, the FDZ width is narrower, i.e. 200–250 m (Fig. 9A, cross-section HH′ and Fig. 10, cross-sections KK′–LL′, and Figs. 5–6). In Macs Knob, where steep (≥25° slope) HW (south of the fault) topographic relief is present and exceeds FW relief far from river valleys, secondary faults are rare and the FDZ width is confined to a surface rupture up to ~100 m wide (Fig. 8B, cross-section FF′, and Figs. 5–6). In areas of low HW and FW topographic relief (e.g., modern stream beds or late Holocene surfaces) the FDZ width is either nearly similar to the former (Fig. 7B, see cross-sections CC′ and DD′) or more confined than the latter (Fig. 7A, cross-section AA′, and Fig. 10A, see the single fault strand near the Hope Shelter, and Figs. 5–6).

The higher differential strikes correlate with the higher differential topographic peaks and the wider FDZ (e.g., east of Macs Knob, the differential strike range is 0°–16°, DT1 peak is 300, DT2 peak is 650, DT3 peak is 700, and the FDZ is up to 500 m wide), and the lower differential strikes correlate with the lower differential topographic peaks and the narrower FDZ (e.g., at Macs Knob, the differential strike range is 0°–7°, DT1 peak is 0, DT2 peak is −300, DT3 peak is −500, and the FDZ is up to 100 m wide) (Fig. 6).

5.5. PSZ subsurface geometry and segmentation

The PSZ strand across Macs Knob bends slightly to the north with increased elevation and in several locations the strand is observed to

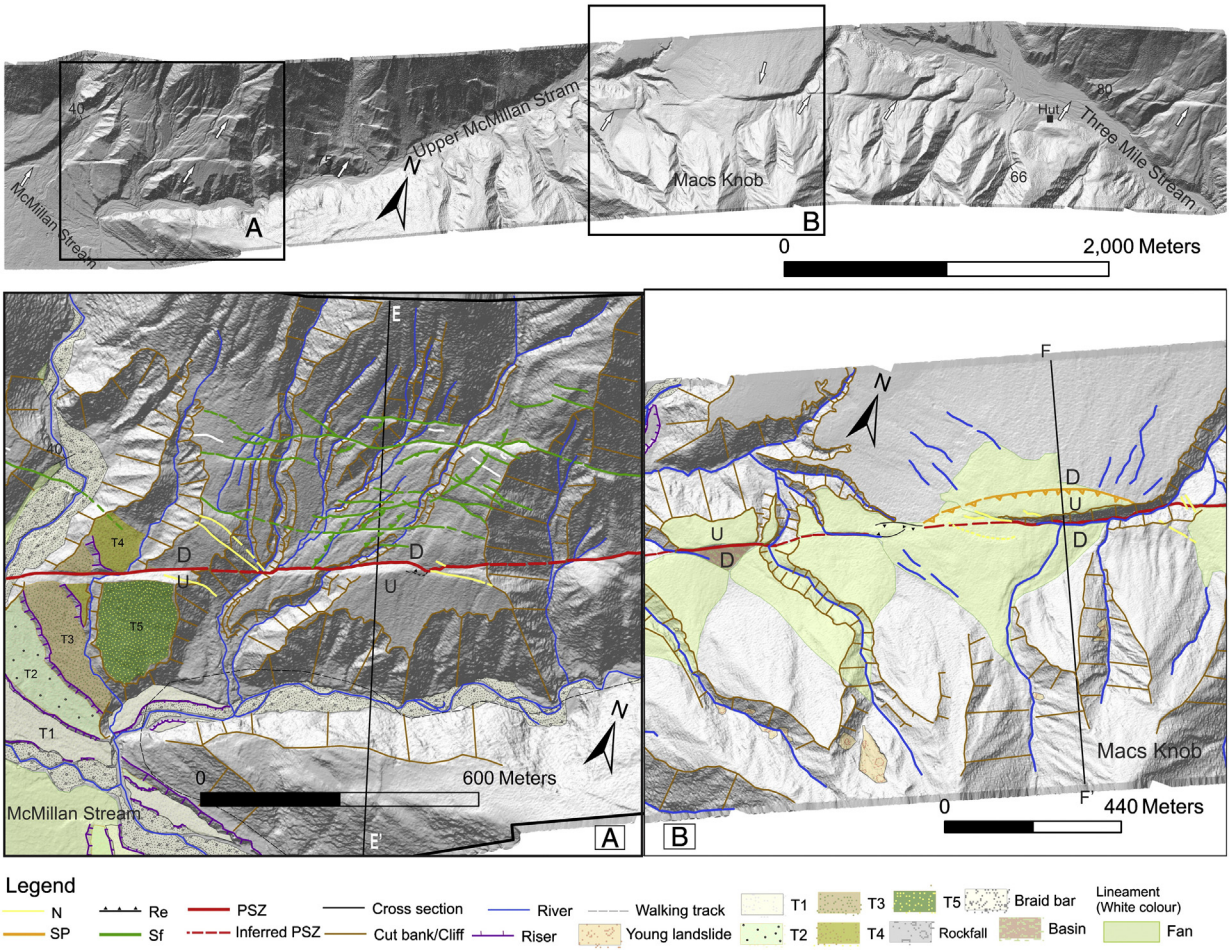

Fig. 8. Uninterpreted LiDAR strip (~7 km long, from McMillan Stream to Three Mile Stream) and structural geomorphic map of the two key sites. Arrows point to the fault strands. (A) East of McMillan Stream and location of cross-section EE′. (B) Macs Knob and location of cross-section FF′.

migrate upstream across stream valley bottoms, indicating a southerly fault dip of this strand (Fig. 8B). Structure contours indicate a dip of 65° SE for the PSZ strand across Macs Knob and 35° SE for the thrust flake. Nearby bedrock shear zones and fractures dip 80–85° S (Langridge, 2004). The cross-section FF′ through Macs Knob presents a model to reconcile these fault orientations, showing a near-surface shallowing in the fault dip (Fig. 11).

The PSZ across Lodge Stream and east of McMillan Stream areas bends slightly to the south with increasing elevation and locally migrates upstream across stream valley bottoms, indicating an overall northerly fault dip (Fig. 9A–B). Structure contours indicate a near-surface fault dip of 60° NW at the Lodge Stream area and 63° NW at the east of McMillan Stream area for the PSZ. The cross-sections in the Three Mile Stream, Macs Knob, east of McMillan stream and Lodge Stream areas portray our interpretation of a shallowing fault dip in the cover deposits compared to the underlying bedrock fault (Figs. 11–12). In these instances the near surface fault dip inferred from PSZ structural contours is shallower than the inferred dip in the underlying bedrock, with a 'downslope rotation' away from the proximal topographic high. The strike continuity of the PSZ trace throughout the Hurunui segment despite different dip directions suggests that the Hurunui segment of the Hope Fault is likely to consist of smaller, oppositely dipping faults (i.e. sub-segments) that are structurally linked and enable through-going rupture propagation. The propagation of coseismic strike-slip ruptures through multiple faults is commonly observed in historical earthquakes (e.g., 2001 Kunlun earthquake, Lin et al., 2003; 1991 Landers earthquake, Sieh et al., 1993; 1999 Hector Mine earthquake; Li et al., 2003).

5.6. Relationship between FDZ width and sediment thickness

The estimated depth-to-bedrock across the FDZ (average thickness of cover integrated over FDZ width) varies from ~0 to 250 m (Figs. 11–12 and Table 3). Fig. 13 shows two diagrams that examine the effect of estimated depths-to-bedrock on the FDZ width, and on the ratio of the amount of fractures/faults to the FDZ width for any particular sample site (cross-section). Fig. 13A shows two different linear correlations; one between cross-sections AA′, FF′ and KK′ and one between the rest of the cross-sections. The smaller group is composed of those cross-sections with the PSZ strikes of 071°–074° and more importantly the strikes of the PSZ segments here show a small variation with the strikes of their adjacent segments (e.g., min. and max. variations are 0°–5°, Table 3). The larger group is composed of those cross-sections with the PSZ strikes of 067°–085° and more importantly the strikes of the PSZ segments here show a bigger variation with the strikes of their adjacent segments (e.g., min. and max. variations are 6°–15°, Table 3). The data from both groups indicate an increase in FDZ width with increased sediment thickness, with an additional role of fault orientation and strike variation. For a constant sediment thickness, significant variation in FDZ width is likely to reflect fault geometry (existence of step-overs or fault bends vs. a long linear PSZ). A

Please cite this article as: Khajavi, N., et al., Influence of topography and basement depth on surface rupture morphology revealed from LiDAR and field mapping, Hope Fault, New Zealand, Tectonophysics (2014), http://dx.doi.org/10.1016/j.tecto.2014.05.032

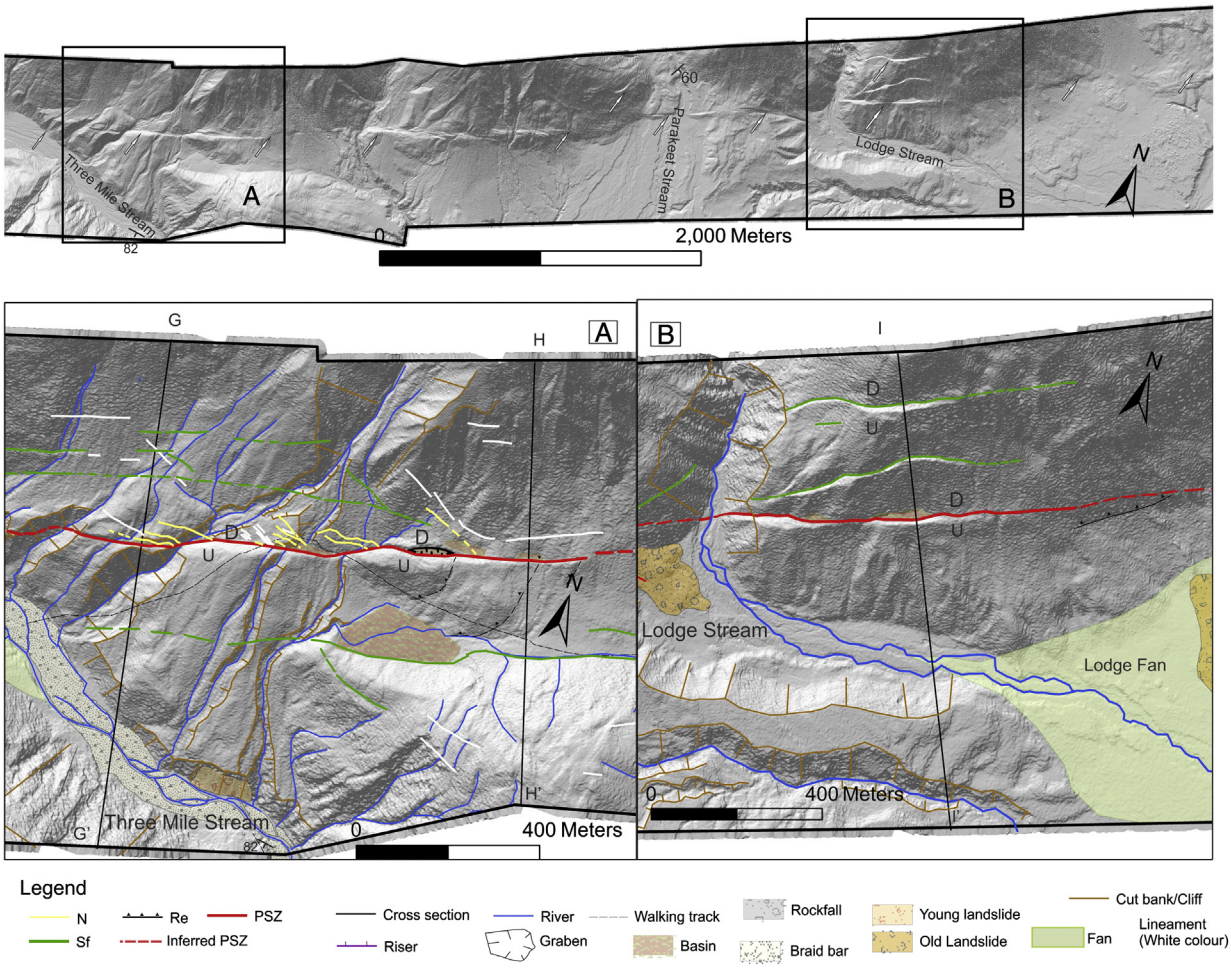

Fig. 9. Uninterpreted LiDAR strip (~7 km long, from Three Mile Stream to Lodge Stream) and structural geomorphic map of the two key sites. Arrows point to the fault strands. (A) East of Three Mile Stream and locations of cross-sections GG′ and HH′. (B) East of Lodge Stream and location of cross-section II′.

partial correlation between the depths to bedrock and the ratio of the number of fault/fractures to the FDZ width is shown on Fig. 13B.

6. Discussion and implications

A comparison of LiDAR fault mapping with the previous field mapping indicates that the use of LiDAR has enabled large improvements in the detection and mapping of the entire FDZ in this densely forested terrain. Our high-resolution mapping of the Hurunui segment surface rupture provides new evidence for previously unknown structures and displacements. Good examples of this include the secondary structures (off the PSZ), the en echelon structures, the gravitational failure scarps, the normal and reverse faults associated with the PSZ, and the displaced terraces and risers to the east of McMillan Stream under thick vegetation (Figs. 7–10). Many of these features had neither been observed from aerial photos, nor seen in the forest during previous reconnaissance studies that focused mainly on the PSZ (e.g., Freund, 1971; Browne, 1987; Langridge, 2004; Langridge and Berryman, 2005). Here, we use the mapped structures as proxies of the fault kinematics and near-surface geometry, and discuss their distribution and abundance in relation to topography, fault strike and thickness of poorly consolidated cover.

6.1. Relationship of fault orientations and kinematics with respect to local and regional stress fields

Transpressive and transtensive faults can be characterized by the angle α (obliquity angle) between the PSZ and the horizontal convergence or extension directions respectively (Woodcock and Fischer, 1986; Cunningham and Mann, 2007; Scholz et al., 2010; Carne and Little, 2012). Analogue models show kinematic and geometric differences between structures forming at low angles of obliquity ($0° \leq \alpha \leq 15°$) and structures forming at high angles of obliquity ($30° \leq \alpha \leq 90°$) (Casas et al., 2001). Where α is ≤15°, deformation is more focused on a steeply dipping (>70°) PSZ and structures are typical of the Riedel model of simple shear (Fig. 3A), but where α is ≥15°, an asymmetric deformation zone is distributed over a shallowly dipping (<40°) PSZ (Casas et al., 2001). This distributed deformation zone could be in the form of uplift resulting from transpression, or in the form of basin resulting from transtension, depending on the stress regime.

With this in mind, our strike analysis of the PSZ strands, using LiDAR data, shows that the primary azimuthal direction of the PSZ (070°–075°) is at an angle of 1°–6° to the Pacific plate slip vector orientation calculated at the fault (249°; DeMets et al., 2010). The Hurunui segment appears as a near-continuous fault along its length on LiDAR with a favourable orientation to transfer strike-slip motion between the Hikurangi subduction zone and the Alpine Fault (Fig. 1). In a general view, the fault is remarkably straight with a gentle curve in its middle (Figs. 2 and 8). We do not observe large-sized basins, uplift zones, or major step-overs. Generally, we observe structures expected for strike-slip systems that are physically connected to the PSZ, and in some areas, a clear superposition of structures is recognized around the PSZ (Fig. 7B). However, the distribution of these structures looks different than the models particularly in terms of fault-normal distribution of structures with respect to the PSZ (Fig. 3A) (e.g., the majority of normal faults are located south of the fault and the majority of reverse

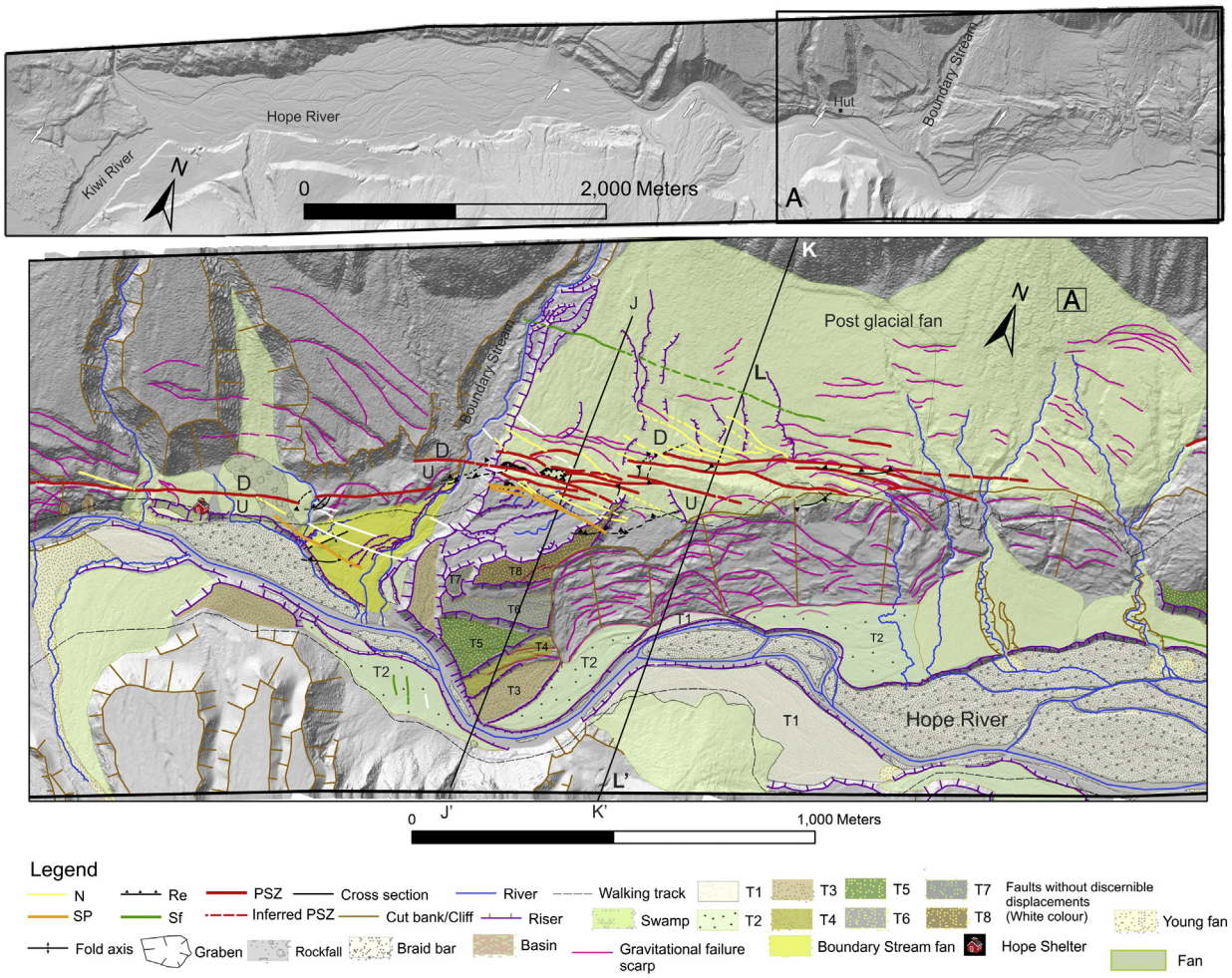

Fig. 10. Uninterpreted LiDAR strip (it is ~8 km long, from Lodge Stream to the eastern extent of the LiDAR swath) and structural geomorphic map of the key site. Arrows point to the fault strands. (A) Hope Shelter and Boundary Stream and locations of cross-sections JJ′, KK′ and LL′.

faults are located north of the fault instead of forming both north and south of the PSZ). Together, the PSZ and structures within the second group (see fault classifications) make a narrower deformation zone of up to ~250 m wide, which is nearly symmetric along the PSZ. However, the entire FDZ including all structures is up to ~500 m wide and definitely asymmetric along the PSZ. Dextral displacements along the PSZ are well preserved and the ratio of horizontal to vertical displacements indicates primarily strike-slip (~7 ± 2:1, Langridge and Berryman, 2005). All of the described characteristics above confirm that the fault is predominantly dextral strike-slip and steeply dipping toward the NW, which is supported by field data (see Methodology section).

Near-fault stress fields may differ from regional stresses (e.g., Holt et al., 2013) due to coseismic slip variations and variations in fault strike and geometry (Lunina et al., 2008), variations in thickness and material properties of faulted media (e.g., Richard et al., 1991, 1995; Norris and Cooper, 1997; Shipton and Cowie, 2003; Barth et al., 2012), and variations in topography (Norris and Cooper, 1995; Eusden et al., 2000, 2005; Barth et al., 2012). Furthermore, fault rotation with progressive displacement can result in cumulative fault kinematic histories that do not directly relate to the present fault orientation and/or slip in the most recent event. The existence of high and variable near-fault surface topography, variable fault strikes and geometries, and variations in sediment thickness adjacent to the Hurunui segment all provide potential influences on near fault stresses in this instance. With this in mind, we use LiDAR-derived orientations and kinematics of the PSZ and normal and dextral-reverse faults connected to the PSZ to derive information about the near-fault stress field.

Assuming that the orientation and kinematics of mapped faults can be used to calculate a strain ellipse that reflects the stress field, and that the σ_2 is vertical in strike-slip faulting, we estimate $\sigma_1 = 100°$–$105°$ and $\sigma_3 = 010°$–$015°$. Geodetic measurements of incremental strain near the Hope Fault used as a proxy for the contemporary stress field indicate σ_1 is oriented between 100° and 110° (Fig. 1; see W vector) (Wallace et al., 2007, 2012). Paleostress tensors derived from focal mechanisms of shallow crustal earthquakes in the northern South Island (Fig. 1; see PHS vector) similarly indicate σ_1 near the Hurunui segment trends 115° (Nicol and Wise, 1992; Pettinga and Wise, 1994). The contemporary stress field calculated by Sibson et al. (2011) using stress inversions from earthquake focal mechanisms shows σ_1 at 115° ± 16° for North Canterbury-Marlborough region. From these data we conclude that the Hurunui segment of the Hope Fault is optimally oriented for dextral strike-slip within the regional stress field.

Mapped normal faults along the Hurunui segment range in length from 18 to 360 m (average = 122 m), have accumulated maximum vertical displacements of 0.2 to 6 m, and have orientations of 095° to 100° (Fig. 4). Where normal fault scarps are present on the youngest parts of the landscape (e.g., on the active alluvial plain of the Hurunui River) adjacent to parts of the PSZ that record only the most recent surface rupture (Langridge et al., 2013), the normal fault lengths are 80 to 85 m, the vertical displacements are 0.2 to 0.5 m, and the orientations are ~100°. Only four of the 70 identified normal faults contain some evidence for dextral displacement, 31 contain features that have not been laterally offset (i.e., have purely dip slip kinematics), and 35 faults do

Please cite this article as: Khajavi, N., et al., Influence of topography and basement depth on surface rupture morphology revealed from LiDAR and field mapping, Hope Fault, New Zealand, Tectonophysics (2014), http://dx.doi.org/10.1016/j.tecto.2014.05.032

Table 2
Characteristics of the deformation zone north and south of the fault. In total, 415 measurements were done. Number, percentage and distribution of measurements north and south of the fault are shown. Detailed classification of the FDZ shows that how much of it is narrower than 100 m, between 100 and 200 m wide, between 300 and 400 m wide, and wider than 400 m north and south of the fault. Along 10% of the PSZ, the FDZ is only limited to the heights of scarps (FDZ is a few metre wide).

			Distribution of the FDZ with respect to the PSZ	Number and percentage of values ≤100 m	Number and percentage of values >100 and ≤200 m	Number and percentage of values >200 and ≤300 m	Number and percentage of values >300 and ≤400 m	Number and percentage of values >400
Measurements of the FDZ width along the fault length (total = 415)	Number of measurements with positive values (north of the fault)	236	57% of the FDZ is located north of the fault	70, 30%	47, 20%	82, 35%	37, 15%	0, 0%
	Number of measurements with negative values (south of the fault)	138	33% of the FDZ is located south of the fault	66, 48%	39, 28%	21, 15%	11, 8%	1, 1%
	Number of measurements where FDZ is equal to the PSZ	41	10% of the PSZ shows FDZ equal to the PSZ	–	–	–	–	–

not contain features that enable assessment of whether lateral displacement is present. In general, it appears that the orientation and kinematics of many of the identified normal faults are best explained by a vertical σ_1, and a σ_3 orientation of 005°–010° that is perpendicular to the regional σ_1 orientation. In particular, the σ_3 orientation derived from single-event normal faults where no near-field variations in topography or sediment thickness are present indicates consistency between the near-fault coseismic and regional stress fields in the absence of local conditions that could perturb the stress field.

Mapped dextral-reverse faults range in length from 8 to 364 m (average = 76 m) with total accumulated maximum slips of 0.5 to 4 m. Thirteen of the 55 identified dextral-reverse faults are associated with pop-up structures, 7 contain features that have not been laterally offset, 10 faults contain features with unambiguous evidence of dextral displacement, and 25 faults do not contain features that enable assessment of whether lateral displacement is present. The average orientation of these faults (055°–065°; Fig. 4) is typically within 5°–20° of the PSZ and 35°–45° of the regional σ_1, consistent with oblique (rather than purely reverse) displacement.

6.2. Sackungen origin for secondary faults?

Sackungen are uphill-facing structures located on the upper parts of mountains and produced by gravitational spreading in slopes (McCalpin, 2003; Li et al., 2010). In the past, this terminology was used for the actual deep-seated gravitational slope deformation that is expressed on the surface by linear features, first introduced by Zischinsky (1966, 1969). McCalpin (2003) introduced three origins for sackungen formation; 1) tectonic origin (resulting from surface faulting), 2) earthquake origin (resulting from coseismic shaking), and 3) neither tectonic nor earthquake origins.

Uphill-facing scarps near the Hope Fault (called mountain faults, or antislope scarps or ridge rents) have been observed by Clayton (1965), Beck (1968) and Freund (1971). Clayton (1965) and Beck (1968) suggested that these features formed due to earthquake shaking on slopes that were oversteepened following LGM, and propagated laterally. Freund (1971) suggested that they are tectonic in origin because they were also observed on low elevation hills and areas where the valleys were lower than threshold steepness.

The secondary faults associated with the Hurunui segment have characteristics implying that they are tectonic in origin: 1) they are preferentially located at lower parts of mountains in a close proximity (i.e. within 300 m) to the PSZ, 2) they are linear, long, and fault-parallel so that they can easily be discriminated from arcuate uphill-facing features occupying higher elevations and slopes (near ridge crests) in the study site, 3) some of them have apparently dextrally displaced streams, 4) they are typically associated with kinematically linked smaller-scale structures, 5) their surface traces occasionally cut through different slopes along strike, which is not typical in the classical definition of sackungen (McCalpin, 2003), and 6) their orientation and kinematics indicate strain orientations consistent with formation by regional stresses (as opposed to topographic stresses alone). We thus attribute these features to tectonic faulting, as opposed to sackungen.

6.3. Topographic influences on near surface fault geometry and surface rupture morphology

In this section we discuss the possibility that topography exerts a fundamental influence on the observed characteristics of the FDZ including the formation of secondary structures. These secondary structures are smaller in size than the second order faults in the study of Barth et al. (2012), and they are more linear than the normal faults shown by Eusden et al. (2000, 2005). We observe that the FDZ is composed of a series of dextral, dextral–normal and normal faults that form negative flower structures. The FDZ is wider both where the strike of the PSZ deflects away from 070° to 075° (Fig. 5) and where mountain flanks have been incised by tributary streams (Figs. 7–10). Moreover, the FDZ has an asymmetric distribution with respect to the PSZ with a wider zone of deformation accommodated where topographic relief is greater. It appears that, where high topography deflects the PSZ in a way to align it with the plate boundary vector, the FDZ is narrowest. However, at many places where high topography locally misaligns segments of the PSZ with the plate boundary vector, the FDZ is wider (Figs. 5 and 14A). This is consistent with the obliquity concept explained by several authors (Woodcock and Fischer, 1986; Cunningham and Mann, 2007; Scholz et al., 2010; Carne and Little, 2012). We suggest that the width of the resulting deformation zone is spatially variable due to two factors; 1) proximity of the PSZ to tributary stream canyons (see Norris and Cooper, 1995, 1997 for the Alpine Fault), and 2) size of the tributary stream canyons (Norris and Cooper, 1995). For example; the FDZ is the widest where the misaligned PSZ segments are near larger stream canyons (like McMillan and Three Mile Streams), narrower where it is near smaller stream canyons (like Parakeet and Lodge Streams), and narrowest where it is more distal to stream canyons (see Fig. 2 for locations, and Figs. 7–10 for explanations). This is in agreement with the stress perturbation concept as streams form canyons that are different from steep mountainous topography elsewhere along the fault.

Topographic relief creates spatial variations in gravitational loads that may perturb near-surface and regional stress fields (McTigue and Mei, 1981; McTigue and Stein, 1984; Savage et al., 1985; Savage and Swolfs, 1986; Liu and Zoback, 1992). McTigue and Mei (1981) used 2D models to compute the magnitude and orientation of the topographically-induced perturbed tectonic stresses in the upper crust. Their results

Please cite this article as: Khajavi, N., et al., Influence of topography and basement depth on surface rupture morphology revealed from LiDAR and field mapping, Hope Fault, New Zealand, Tectonophysics (2014), http://dx.doi.org/10.1016/j.tecto.2014.05.032

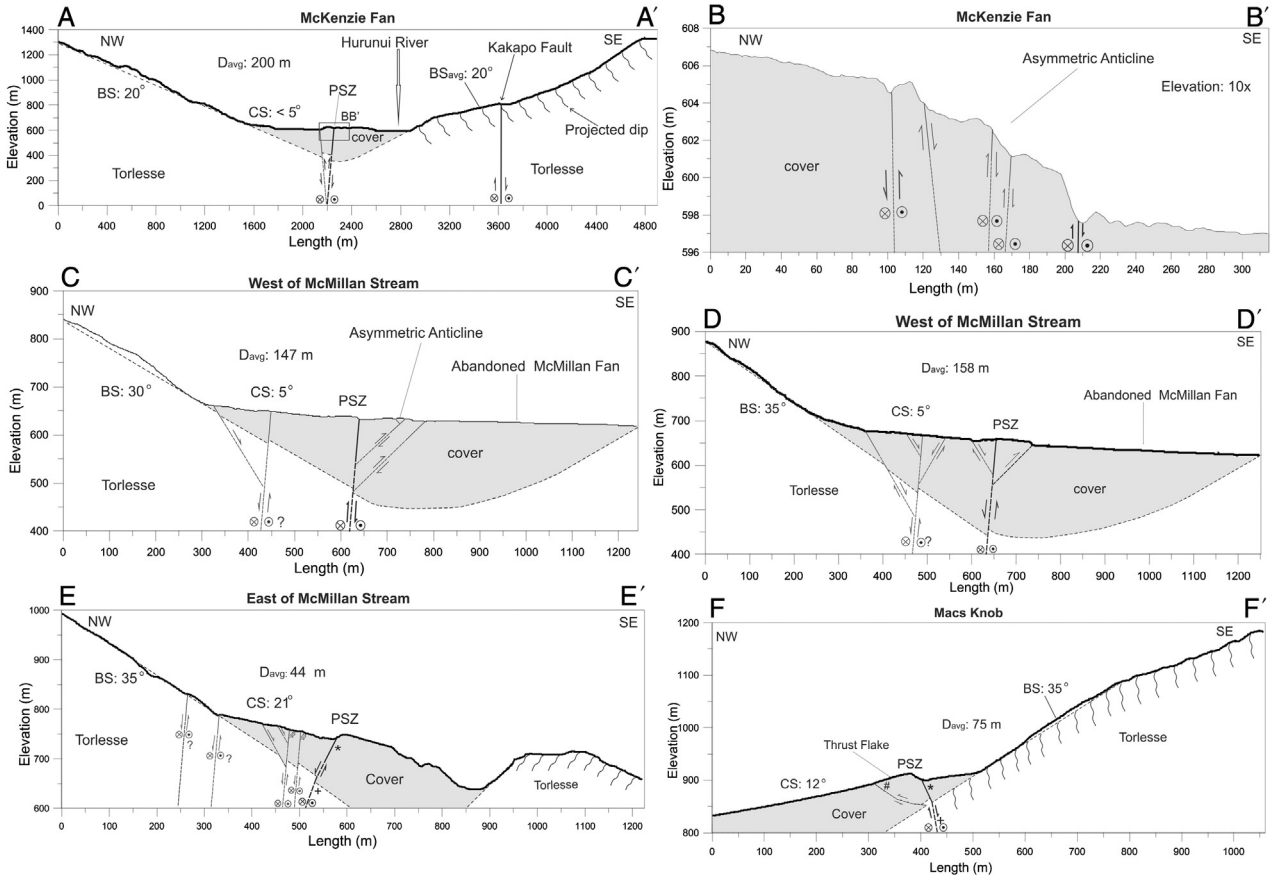

Fig. 11. Cross-sections AA′ to FF′ showing fault models at depth. Dip angle of the PSZ considered being 85° in both bedrock and covering deposits where no other data were available. Abbreviations: BS: Bedrock Slope, CS: Cover Slope, D_{avg}: average depth of the cover deposits beneath the FDZ. Symbols in cross-section EE′: +, dip angle of 70° NW for the PSZ measured from bedrock in the field by Langridge (2004), *, dip angle of 63° NW for the PSZ measured from LiDAR-derived structural contours. Symbols in cross-section FF′: *, dip angle of 65° SE for the PSZ measured from LiDAR-derived structural contours, #, dip angle of 35° SE for the thrust flake measured from LiDAR-derived structural contours, +, dip angle of 80° SE for the PSZ measured from bedrock in the field by Langridge (2004).

suggested that regional horizontal compression can be modified (decreased or changed to tension) in the proximity of high topography. Savage et al. (1985) modelled the near-surface gravity-induced stresses for isolated symmetric ridge and valley. Their results revealed that horizontal compressive stresses form near the ridge top and decline with increasing Poisson's ratio. In comparison, horizontal tensile stresses form beneath the valley, however, they reduce and change to compressive with increasing Poisson's ratio. They also showed that the magnitude of the gravity-induced stresses is approximately equal to ρgb, where ρ is the mass per unit volume, g is the gravitational acceleration, and b is the height of the ridge or the depth of the valley. Savage and Swolfs (1986) modelled the effect of tectonic and gravitational stress in long symmetric ridges and valleys. Their results also showed that topography decreases regional tectonic compression near the ridge top and can change it to tension where the slope is steep, but the regional tectonic stress focuses in the valleys. When the effect of topography on regional tectonic stresses is added to the effect of topography on gravitational stresses, the lateral components of the gravity-induced compressive stress at the ridge top are slightly increased while the gravity-induced tensile stress beneath the valley is slightly decreased (Savage and Swolfs, 1986). Norris and Cooper (1995, 1997) also discussed the effect of topographically perturbed stresses on developing serial and parallel partitioning of the central segment of the dextral-reverse Alpine Fault and suggested a depth of 1–4 km for stress perturbation around the fault (they considered the depth of stress disturbance to be one to two times the valley relief (Savage and Swolfs, 1986)). In all of the above studies, the relationship between topographic relief and the FDZ width has not been investigated specifically, however mechanistic explanations linking topography with the state of stress on and around faults are presented.

We argue based on our mapping data that if the zone of high shear stress on the valley sides is strong enough, it can rotate the fault plane, thereby influencing rupture propagation and possibly causing fault bifurcation into separate segments, resulting in enhanced fault geometric complexities and increasing deformation zone width. The local valley relief adjacent to the Hurunui segment is 700–1100 m (Fig. 6) suggesting that the near-fault stress field could be perturbed to depths of ~1–2 km. Our modelled cross-sections using field data show that shallower (<85°) dip angles of the PSZ (e.g., 63°, cross-section EE′ and 65° cross-section FF′), occur in cover deposits at depths generally <100–200 m, although we cannot dismiss the possibility of additional fault rotation at depth. Our results strongly suggest that the Hurunui segment is dominantly strike-slip with a dip angle of ~85° NW at depth (along much of its length) or SE at a shallower depth (in Macs Knob), but can appear as a dextral-reverse or dextral–normal fault with dip angle of 60°–65° near the surface depending on the existence of high topography south or north of the fault or thickness of deposits. The existence of an asymmetric FDZ along the PSZ also confirms the fault should be dipping more gently near the surface especially where it enters the cover deposits. The secondary faults are mostly parallel to sub-parallel to the PSZ, uphill-facing, small scale (average length = 160 m with only two of them being around 2 km long), and are only up to 500 m off the PSZ. They are likely to join with the dextral strike-slip PSZ at a shallow depth. If we project the faults downdip with

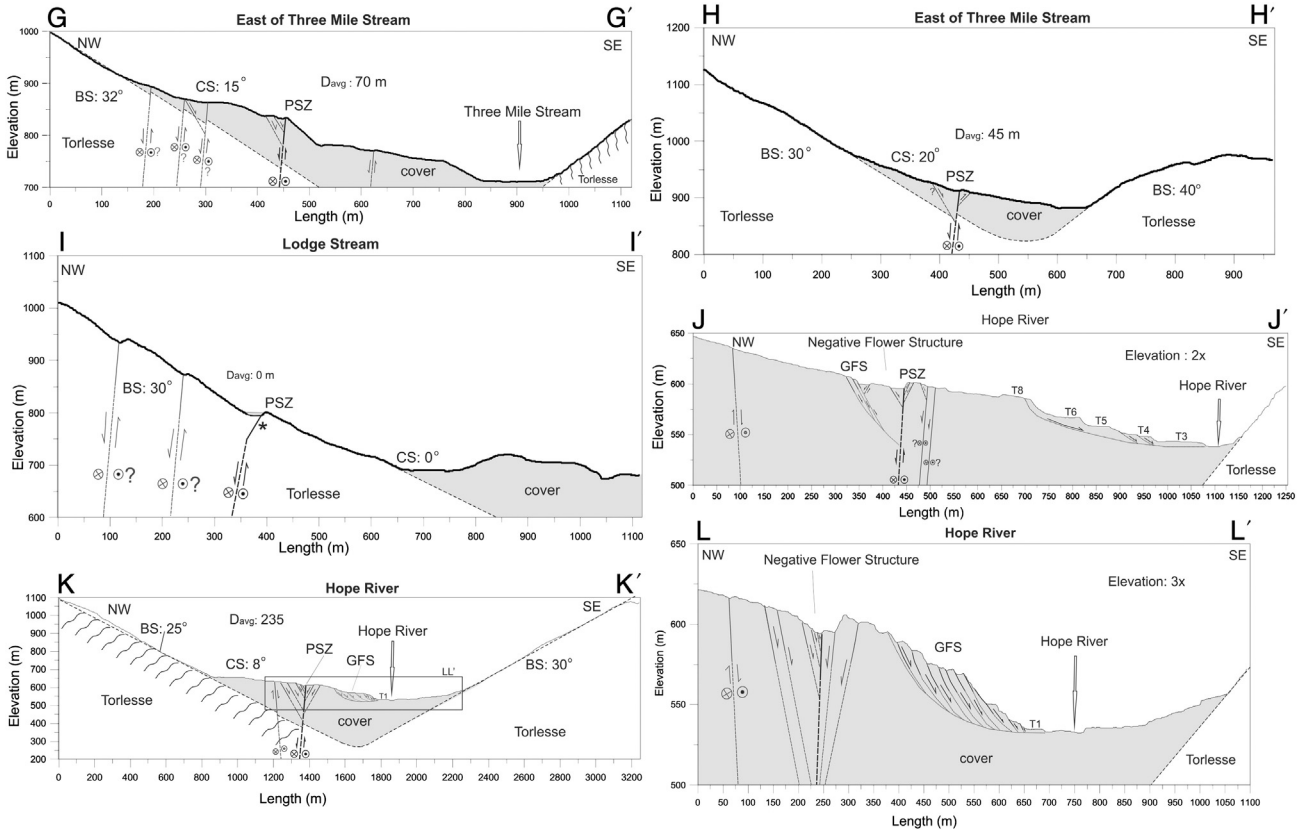

Fig. 12. Cross-sections GG′ to LL′ showing fault models at depth. Dip angle of the PSZ is considered to be 85° in both bedrock and cover deposits where no other data were available. Abbreviations: BS: Bedrock Slope, CS: Cover Slope, D_{avg}: average depth of the cover deposits beneath the FDZ, GFS: Gravity Failure Scarps. Symbol * in cross-section II′: dip angle of 60° NW for the PSZ measured from LiDAR-derived structural contours.

the dip angles assumed in the methodology section, both the faults that are connected to the PSZ on the surface (e.g., normal and dextral- reverse faults) and the very small-scale faults that are connected to the secondary faults on the surface merge into a single PSZ strand or into their relevant major secondary fault at depths of ~50–200 m (see cross-sections BB′, CC′, DD′, EE′, FF′, GG′, JJ′ and KK′). In contrast, the larger dextral strike-slip secondary and splay faults (see other near-vertical dextral faults around the PSZ; cross-sections AA′, CC′, DD′, EE′, GG′, II′, JJ′, and KK′) would merge with the PSZ at deeper depths beyond our cross-sectional views. This is consistent with our suggestion of the stress perturbation depth around the fault in this area. The subsurface interaction of the majority of the faults (the branching depth) in most instances seems to be close to, or at the basement-cover interface, i.e., 50–200 m depth.

Scarps associated with some of the secondary faults range from ~0.1 to 6 m in height. The vertical single event displacement (along the PSZ) and recurrence interval time of the Hurunui segment, calculated by Langridge and Berryman (2005), are ~0.2 m and 300–500 years respectively. Therefore, some of the secondary faults with large vertical slip have likely ruptured and/or reactivated during multiple events, i.e., being coseismic features. It appears that at least many of them are well-established structures that accommodate slip during earthquake ruptures. The characteristics of many of the secondary features observed here are not consistent with the post-seismic collapse features documented by Eusden et al. (2000, 2005) (see supplementary file; part 3.2). In contrast, their characteristics are consistent with the mapped and interpreted coseismic dextral–normal faults (third order faults) associated with the Alpine Fault (e.g., similar surface patterns and lengths, no cross-cutting relationship between the faults, locating on the range-ward side of the fault, large uphill-facing scarps) (Barth et al., 2012).

The results of this study show that topography extending to fault-normal distances up to 1.5 km is important in influencing the morphologic properties of the FDZ. At locations where DT1 is around 0, but DT2 and DT3 yield highly positive or negative values, a relatively wide FDZ is still recorded. Topographic profiles DT1, DT2 and DT3 (Fig. 6), all show that north of the PSZ is higher in elevation than south of it. The only exception is the Macs Knob region, in which higher mountains are south of the PSZ. We observe a strong correlation between the upthrown side of the fault and high topography along the entire length of the Hurunui segment, i.e., scarps are uphill-facing. We present a model (3D block diagram in Fig. 14A–B, see figure description) to explain the fault kinematics. In our model, high topography exerts a load on the fault plane and forces it to deflect away from the mountains. By variably loading the PSZ by differential topography along strike, the fault strike will vary and its dip can no longer remain very steep at very shallow depth near the base or on the flanks of the mountain so that it branches off to adjust itself and accommodate the local oblique motion exerted by topography. This model explains the production of uphill-facing scarps. Our model and the results of our geomorphic mapping and topographic analysis suggest that the surface geometry of the PSZ and FDZ is locally controlled and independent of large-scale regional stress.

6.4. Depth-to-bedrock influence on surface rupture morphology

Field observations (e.g., Kunlun earthquake, Lin et al., 2003; El Mayor–Cucapah earthquake, Oskin et al., 2012) and models (e.g., Richard et al., 1991, 1995) indicate that fault zones are typically wider in unconsolidated cover deposits compared to consolidated deposits and basement rocks. The results of our study indicate that the

Table 3
Structural and morphological characteristics of the cross-sections.

Cross-sections and comments	Fault strike	Average depth of cover deposits under the PSZ	Fault density (no)	FDZ width	Slope
AA′–BB′ Right step-over, 3° change in strike, situated in valley	74°	200	5	107 at the cross-section	<5°
CC′ 10° fault bend, situated in valley	64°–74°	147	6	443	5°
DD′ Left step-over, 8° change in strike, situated in valley	67	158	6	400	5°
EE′ Situated at the mountain flank, near 2 large branches of McMillan Stream and some smaller tributaries	68	44	9	330	21°
FF′ Situated at the mountain flank, oldest part of the landscape, nearly at the same distance to McMillan and Three Mile Stream (not very close to large streams)	71	75	2	83	12°
GG′ Left step-over, 9° change in strike, situated at the mountain flank, near Three Mile Stream and its tributaries	73	70	8	434	15°
HH′ Left step-over, 6° change in strike, situated at the mountain flank, not very close to Three Mile Stream and its tributaries	73	45	4	215	20°
II′ Left step-over, 10° change in strike, situated at the mountain flank, near Lodge Stream	69	0	3	284	30°
JJ′ Left step-over, 15° bend, en echelon structures, situated at the mountain flank, near Boundary Stream and Hope River	85	235?	11	420	8°
KK′ En echelon structures, 5° change in strike of the main PSZ strands, situated at the mountain flank, at a greater distance to Boundary Stream (with respect to JJ′) and near Hope River	72	235	9	254	8°

thickness of the unconsolidated cover deposits is an important factor in influencing the FDZ width. However, the wide FDZ exposed along the cross-sections CC′, DD′, EE′, GG′, HH′, and JJ′ (Figs. 11–12 and Table 3) is not only a result of the thickness of cover deposits, but also related to the changes in fault strike (6°–15°) where there are step-overs or bends. The changes in the strike of the fault are resulted from different responses of the fault to the existing variable topography along it. Therefore, we believe that the thickness of cover deposits is a second order control (after topography relief) on the FDZ both at the flanks of mountains and adjacent to valleys. The latter implies that the existence of the fault step-overs or bends along the strike of the fault is the first order control on the FDZ (e.g., McKenzie and McMillan sites; Fig. 7A–B). An important first order control of topography is also illustrated by the 1888 Hope Fault rupture; the surface rupture is comparably narrow and straight where it traverses areas with minimal surface relief (i.e. no topographic loading) despite significant thicknesses of underlying unconsolidated outwash deposits, and is more complex (more fault step-overs and/or bends) in areas of higher topographic relief (Cowan, 1990; Cowan and McGlone, 1991).

6.5. Fault maturity, FDZ width, slip measurements, and paleoseismic implications

The Hope Fault is a structurally mature (Cowan et al., 1996), well-established and fast-slipping active fault with a recurrence interval of ~180–500 years (Cowan and McGlone, 1991; Langridge et al., 2003; Langridge and Berryman, 2005; Langridge et al., 2013). Despite this, deformation zones of up to ~2 km wide including transpressive wedges along the Conway segment (Eusden et al., 2000, 2005), and up to 2.3 km wide including depressions and constraining bends along the Hope River segment (Freund, 1971; Cowan, 1989, 1990), and up to ~500 m wide including secondary structures along the Hurunui segment (this study) have been identified. As shown in Table 1, other mature strike-slip faults can also develop wide deformation zones. Therefore, it is important to study the key controlling factors, except the existence of step-overs or bends (fault complex geometries), on the rupture patterns and to investigate if there is a similar pattern.

In this study, we illustrate that along-strike variability in FDZ width and surface rupture complexity reflects variations in topographic loading and sediment thickness that alter the near-fault stress fields, fault geometries, and mechanical properties of the faulted substrate at shallow (<1–2 km) depths. Significant near surface rupture complexity and possible variations in surface slip on any given structure may result despite simple, uniform slip on a confined, structurally simple underlying fault at seismogenic depths (e.g., Graymer et al., 2007). For this reason, it is possible in some instances that the total finite slip measured in previous investigations may not have captured all of the total displacement that was measured on the LiDAR. Furthermore, we do not account for possible distributed deformation that was not reflected by discrete surface rupture (e.g., Quigley et al., 2010, 2012; Van Dissen et al., 2011). As a consequence, previous slip rates estimated using slip measurements limited to the PSZ alone may have underestimated the slip rate in some instances along the Hope Fault (see also Oskin et al., 2012 as an example for the El Mayor–Cucapah surface rupture).

7. Conclusions

Quantitative and detailed LiDAR-derived mapping presented in this work confirm the value of LiDAR as a robust tool for the detailed mapping of fault structures under forest cover. Field-based studies, orthophotos and aerial images also played an important role in our fault and geomorphic mapping and interpretation. A detailed structural geomorphic map was produced for the entire LiDAR strip in this study. Our study reveals that the Hurunui segment of the Hope Fault trends 070°–075° and is favourably oriented for dextral strike slip with respect to the orientation of the Pacific plate slip vector. The fault has evolved as a spatially diverse deformation zone that varies in width from a few metres to up to 500 m. This deformation zone has locally been controlled by the oblique component of slip resulting from topographic loading on the fault plane and deflecting it from its favourable orientation for strike-slip motion, the proximity of the fault to the major river valleys

Please cite this article as: Khajavi, N., et al., Influence of topography and basement depth on surface rupture morphology revealed from LiDAR and field mapping, Hope Fault, New Zealand, Tectonophysics (2014), http://dx.doi.org/10.1016/j.tecto.2014.05.032

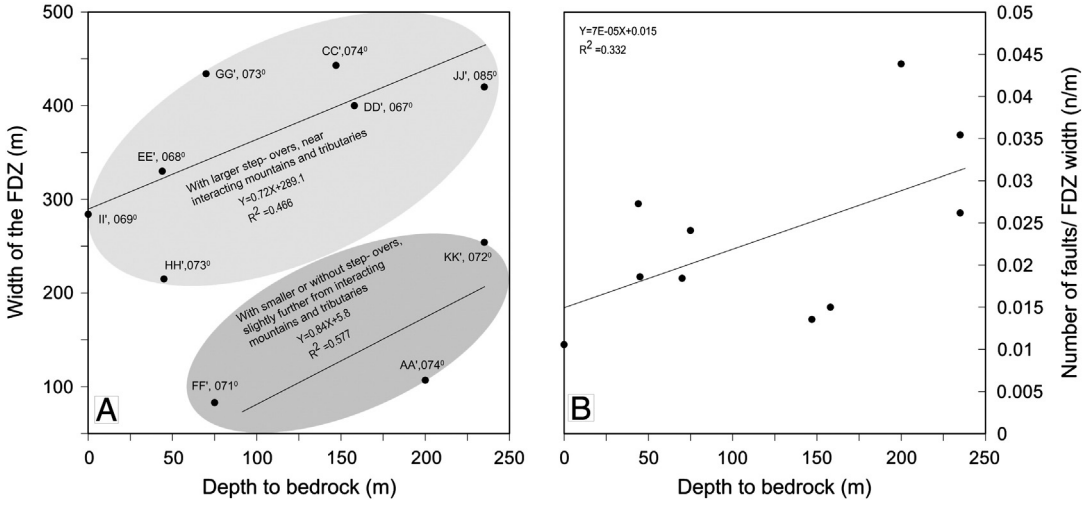

Fig. 13. Impact of average depth of the cover deposits beneath the FDZ on the FDZ width and fault density within the FDZ. (A) Two groups of cross-sections with correlations between their samples are identified. These groups have different characteristics (see Table 3 and comments related to each cross-section). Cross-sections are presented with their ID and the strike of the PSZ strand. For example: AA, 074° means that cross-section AA′ includes a PSZ strand that strikes 074°. (B) A partial relationship appears between the average depth-to-bedrock beneath the PSZ and the number of faults included within the FDZ in each cross-section.

and thickness of cover deposits. Large displacements on the structures forming the FDZ record multiple earthquakes since the late Pleistocene. The normal and dextral-reverse faults join with the dextral strike-slip PSZ close to, or at the basement-cover interface, i.e., ~50–200 m depth, indicating that the surface rupture zone complexity results from shallow (<1–2 km) fault zone widening and bifurcation. The PSZ-parallel to -subparallel dextral secondary structures (average length = 160 m) forming wedges and dextral strike-slip splay faults

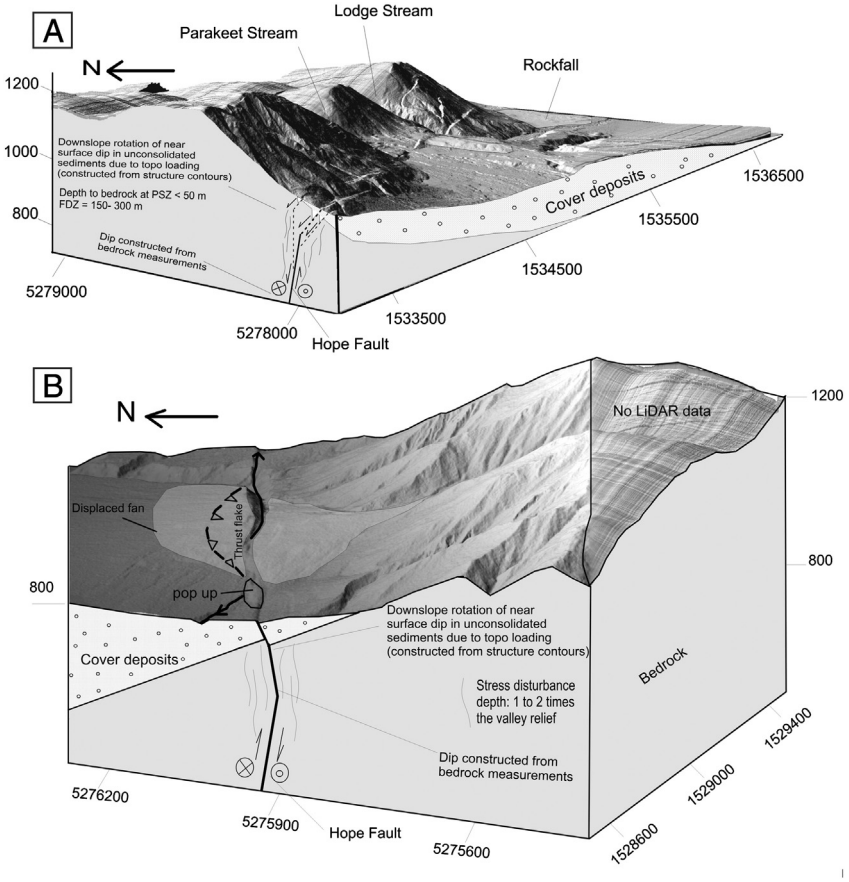

Fig. 14. 3-D models of small portions of the LiDAR swath showing fault branching depths where the fault cuts flanks of mountains. The block diagrams were built using xyz LiDAR data and Surfer software. Note that all of the fault scarps are uphill-facing. We interpret that the fault escapes from topography as it propagates through the surface. (A) Parakeet site; high topography is north of the fault, more branching occurs where topography misaligned the fault strike with the regional stress orientation, deeper branching occurs in bedrock. (B) Macs Knob site; high topography is south of the fault, no deep branching occurs in bedrock because topography aligned the fault strike with the regional stress orientation and this site is the oldest part of the landscape (slip has been localized on a single fault strand over time), the branching depth is limited to the thickness of cover deposits (see cross-section FF′).

Please cite this article as: Khajavi, N., et al., Influence of topography and basement depth on surface rupture morphology revealed from LiDAR and field mapping, Hope Fault, New Zealand, Tectonophysics (2014), http://dx.doi.org/10.1016/j.tecto.2014.05.032

could possibly merge with the dextral strike-slip PSZ at depths that are still within the expected penetration depth of topographically-influenced stress perturbations.

Acknowledgements

We wish to thank NZ Natural Hazards Research Platform Grant 2010-GNS-01-NHRP and the New Zealand Earthquake Commission Capability Fund for funding this research. We thank the Department of Conservation and land owner of the Poplar Station Kevin Henderson for site access. We thank our field assistants Amir Rezanejad and Fidel Martín González and acknowledge Jocelyn Campbell, Chris Smart, Jarg Pettinga, Brendan Duffy, and Nic Barth for academic discussions. We also thank Mike Oskin and An Yin for constructive comments on this manuscript.

Appendix A. Supplementary data

Supplementary data associated with this article can be found in the online version, at http://dx.doi.org/10.1016/j.tecto.2014.05.032. These data include Google map of the most important areas described in this article.

References

Arrowsmith, J.R., Zielke, O., 2009. Tectonic geomorphology of the San Andreas Fault zone from high resolution topography: an example from the Cholame segment. Geomorphology 113, 70–81.
Aydin, A., Schultz, R.A., 1990. Effect of mechanical interaction on the development of strike-slip faults with echelon patterns. J. Struct. Geol. 12, 123–129.
Azzaro, R., Branca, S., Gwinner, K., Coltelli, M., 2012. The volcano-tectonic map of Etna volcano, 1:100.000 scale: an integrated approach based on a morphotectonic analysis from high-resolution DEM constrained by geologic, active faulting and seismotectonic data. Ital. J. Geosci. 131, 153–170.
Barka, A., Akyüz, H.S., Altunel, E., Sunal, G., Çakir, Z., Dikbas, A., Yerli, B., Armijo, R., Meyer, B., De Chabalier, J.B., Rockwell, T., Dolan, J.R., Hartleb, R., Dawson, T., Christofferson, S., Tucker, A., Fumal, T., Langridge, R., Stenner, H., Lettis, W., Bachhuber, J., Page, W., 2002. The surface rupture and slip distribution of the 17 August 1999 İzmit earthquake (M 7.4), North Anatolian fault. Bull. Seismol. Soc. Am. 92, 43–60.
Barrell, D.J.A., Townsend, D.B., 2012. General distribution and characteristics of active faults and folds in the Hurunui District. North Canterbury GNS Science Consultancy Report 2012/113 (45 pp.).
Barth, N.C., 2013. A Tectono-Geomorphic Study of the Alpine Fault, New Zealand, Geological Sciences. University of Otago, Dunedin, p. 319.
Barth, N.C., Toy, V.G., Langridge, R.M., Norris, R.J., 2012. Scale dependence of oblique plate-boundary partitioning: new insights from LiDAR, central Alpine fault, New Zealand. Lithosphere. http://dx.doi.org/10.1130/L201.1.
Beauprêtre, S., Garambois, S., Manighetti, I., Malavieille, J., Sénéchal, G., Chatton, M., Davies, T., Larroque, C., Rousset, D., Cotte, N., Romano, C., 2012. Finding the buried record of past earthquakes with GPR-based palaeoseismology: a case study on the Hope fault, New Zealand. Geophys. J. Int. 189, 73–100.
Beavan, J., Tregoning, P., Bevis, M., Kato, T., Meertens, C., 2002. Motion and rigidity of the Pacific Plate and implications for plate boundary deformation. J. Geophys. Res. 107 (B10).
Beck, A.C., 1968. Gravity faulting as a mechanism of topographic adjustment. N. Z. J. Geol. Geophys. 11, 191–199.
Begg, J.G., Mouslopoulou, V., 2010. Analysis of late Holocene faulting within an active rift using lidar, Taupo Rift, New Zealand. J. Volcanol. Geotherm. Res. 190, 152–167.
Benson, A.M., Little, T.A., Van Dissen, R.J., Hill, N., Townsend, D.B., 2001. Late Quaternary paleoseismic history and surface rupture characteristics of the Eastern Awatere strike-slip fault, New Zealand. Bull. Geol. Soc. Am. 113, 1079–1091.
Ben-Zion, Y., Andrews, D.J., 1998. Properties and implications of dynamic rupture along a material interface. Bull. Seismol. Soc. Am. 88, 1085–1094.
Berryman, K., Beanland, S., 1991. Variation in fault behaviour in different tectonic provinces of New Zealand. J. Struct. Geol. 13, 177–189.
Berryman, K.R., Beanland, S., Cooper, A.F., Cutten, H.N., Norris, R.J., Wood, P.R., 1992. The Alpine Fault, New Zealand: variation in Quaternary structural style and geomorphic expression. Ann. Tecton. 6, 126–163.
Berryman, K.R., Rattenbury, M., Isaac, M., Villamor, P., Van Dissen, R., 2003. Active Faulting and Strain at the Junction of the Alpine and Hope Faults. Geological Society of New Zealand Miscellaneous Publication 116A, New Zealand, p. 18.
Binet, R., Bollinger, L., 2005. Horizontal coseismic deformation of the 2003 Bam (Iran) earthquake measured from SPOT-5 THR satellite imagery. Geophys. Res. Lett. 32, L02307.
Bowen, F.E., 1964. Sheet 15- Buller. Geological Map of New Zealand 1:250000, Wellington, New Zealand, Department of Scientific and Research.
Browne, G.H., 1987. Geological comments on the Lake Sumner-Harper Pass area, Southern Alps. Immediate Report. New Zealand Geological Survey, Christchurch.
Browne, G.H., 1992. The northeastern portion of the Clarence Fault: tectonic implications for the late Neogene evolution of Marlborough, New Zealand. N. Z. J. Geol. Geophys. 35, 437–445.
Burbank, D.W., Anderson, R.S., 2006. Tectonic Geomorphology, 5 ed. Blackwell Science Ltd., p. 304.
Carne, R.C., Little, T.A., 2012. Geometry and scale of fault segmentation and deformational bulging along an active oblique-slip fault (Wairarapa fault, New Zealand). Geol. Soc. Am. Bull. 124, 1365–1381.
Casas, A.M., Gapais, D., Nalpas, T., Besnard, K., Román-Berdiel, T., 2001. Analogue models of transpressive systems. J. Struct. Geol. 23, 733–743.
Chan, Y.C., Chen, Y.G., Shih, T.Y., Huang, C., 2007. Characterizing the Hsincheng active fault in northern Taiwan using airborne LiDAR data: detailed geomorphic features and their structural implications. J. Asian Earth Sci. 31, 303–316.
Clayton, L.S., 1965. Late Pleistocene Geology of the Waiau Valley, North Canterbury, New Zealand. University of Illinois, Urbana, p. 91.
Cowan, H.A., 1989. An Evaluation of the Late Quaternary Displacements and Seismic Hazard Associated with the Hope and Kakapou faults, Amuri District, North Canterbury, Geological Sciences. University of Canterbury, Christchurch, p. 239.
Cowan, H.A., 1990. Late Quaternary displacements on the Hope Fault at Glynn Wye, North Canterbury. N. Z. J. Geol. Geophys. 33, 285–293.
Cowan, H.A., 1991. The North Canterbury earthquake of September 1, 1888. J. R. Soc. N. Z. 21, 1–12.
Cowan, H.A., McGlone, M.S., 1991. Late Holocene displacements and characteristic earthquakes on the Hope River segment of the Hope Fault, New Zealand. J. R. Soc. N. Z. 21, 373–384.
Cowan, H., Nicol, A., Tonkin, P., 1996. A comparison of historical and paleoseismicity in a newly formed fault zone and a mature fault zone, North Canterbury, New Zealand. J. Geophys. Res. Solid Earth 101, 6021–6036.
Cunningham, W.D., Mann, P., 2007. Tectonics of strike-slip restraining and releasing bends. Geol. Soc. Lond., Spec. Publ. 290, 1–12.
DeMets, C., Gordon, R.G., Argus, D.F., Stein, S., 1994. Effect of recent revisions to the geomagnetic reversal time scale on estimates of current plate motions. Geophys. Res. Lett. 21, 2191–2194.
DeMets, C., Gordon, R.G., Argus, D.F., 2010. Geologically current plate motions. Geophys. J. Int. 181, 1–80.
Dorsey, R.J., 2002. Stratigraphic record of Pleistocene initiation and slip on the Coyote Creek fault, Lower Coyote Creek, southern California. Geol. Soc. Am. Spec. Pap. 365, 251–269.
Duffy, B., Quigley, M., Barrell, D.J.A., Van Dissen, R., Stahl, T., Leprince, S., McInnes, C., Bilderback, E., 2013. Fault kinematics and surface deformation across a releasing bend during the 2010 MW 7.1 Darfield, New Zealand, earthquake revealed by differential LiDAR and cadastral surveying. Geol. Soc. Am. Bull. 125, 420–431.
Elliott, A.J., Dolan, J.F., Oglesby, D.D., 2009. Evidence from coseismic slip gradients for dynamic control on rupture propagation and arrest through stepovers. J. Geophys. Res. Solid Earth 114, B02313.
Eusden, J.D., Pettinga, J.R., Campbell, J.K., 2000. Structural evolution and landscape development of a collapsed transpressive duplex on the Hope Fault, North Canterbury, New Zealand. N. Z. J. Geol. Geophys. 43, 391–404.
Eusden, J.D., Pettinga, J.R., Campbell, J.K., 2005. Structural collapse of a transpressive hanging-wall fault wedge, Charwell region of the Hope Fault, South Island, New Zealand. N. Z. J. Geol. Geophys. 48, 295–309.
Freund, R., 1971. The Hope Fault: a strike-slip fault in New Zealand. N. Z. Geol. Surv. Bull. 86, 49 p.
Gold, R.D., Stephenson, W.J., Odum, J.K., Briggs, R.W., Crone, A.J., Angster, S.J., 2013. Concealed Quaternary strike-slip fault resolved with airborne lidar and seismic reflection: the Grizzly Valley fault system, northern Walker Lane, California. J. Geophys. Res. Solid Earth 118, 3753–3766.
Graymer, R.W., Langenheim, V.E., Simpson, R.W., Jachens, R.C., Ponce, D.A., 2007. Relatively simple through-going fault planes at large-earthquake depth may be concealed by the surface complexity of strike-slip faults. Geol. Soc. Lond., Spec. Publ. 290 (1), 189–201.
Gregg, D.R., 1964. Sheet 18- Hurunui. Geological Map of New Zealand 1:250000, Wellington, New Zealand, Department of Scientific and Industrial Research.
Haddad, D.E., Akçiz, S.O., Arrowsmith, J.R., Rhodes, D.D., Oldow, J.S., Zielke, O., Toké, N.A., Haddad, A.G., Mauer, J., Shilpakar, P., 2012. Applications of airborne and terrestrial laser scanning to paleoseismology. Geosphere 8, 771–786.
Hanks, T.C., Kanamori, H., 1979. Fault mechanics. J. Geophys. Res. Solid Earth 84, 2145.
Holt, R.A., Savage, M.K., Townend, J., Syracuse, E.M., Thurber, C.H., 2013. Crustal stress and fault strength in the Canterbury Plains, New Zealand. Earth Planet. Sci. Lett. 383, 173–181.
Honegger, D.G., Nyman, D.J., Johnson, E.R., Cluff, L.S., Sorensen, S.P., 2004. Trans-Alaska Pipeline System Performance in the 2002 Denali Fault, Alaska, Earthquake. Earthquake Spectra 20, 707–738.
Hreinsdóttir, S., Freymueller, J.T., Bürgmann, R., Mitchell, J., 2006. Coseismic deformation of the 2002 Denali Fault earthquake: insights from GPS measurements. J. Geophys. Res. Solid Earth 111, B03308.
Jackson, J., Bouchon, M., Fielding, E., Funning, G., Ghorashi, M., Hatzfeld, D., Nazari, H., Parsons, B., Priestley, K., Talebian, M., Tatar, M., Walker, R., Wright, T., 2006. Seismotectonic, rupture process, and earthquake-hazard aspects of the 2003 December 26 Bam, Iran, earthquake. Geophys. J. Int. 166, 1270–1292.
Joussineau, G., Aydin, A., 2009. Segmentation along strike-slip faults revisited. Pure Appl. Geophys. 166, 1575–1594.
Khajavi, N., Langridge, R., Quigley, M., 2014. The 1888 Amuri earthquake and paleoseismicity of the western Hope Fault, New Zealand: Implications for Fault Segmentation, (in preparation).
Kim, Y.S., Peacock, D.C.P., Sanderson, D.J., 2004. Fault damage zones. J. Struct. Geol. 26, 503–517.

Please cite this article as: Khajavi, N., et al., Influence of topography and basement depth on surface rupture morphology revealed from LiDAR and field mapping, Hope Fault, New Zealand, Tectonophysics (2014), http://dx.doi.org/10.1016/j.tecto.2014.05.032

Knuepfer, P.L.K., 1992. Temporal variations in latest Quaternary slip across the Australian–Pacific plate boundary, northeastern South Island, New Zealand. Tectonics 11, 449–464.

Langridge, R., 2004. How is tectonic slip partitioned from the Alpine Fault to the Marlborough Fault System?—results from the Hope Fault. Institute of Geological & Nuclear Sciences Science Report 2004/32 (18 pp.).

Langridge, R.M., Berryman, K.R., 2005. Morphology and slip rate of the Hurunui section of the Hope Fault, South Island, New Zealand. N. Z. J. Geol. Geophys. 48, 43–57.

Langridge, R., Campbell, J., Hill, N., Pere, V., Pope, J., Pettinga, J., Estrada, B., Berryman, K., 2003. Paleoseismology and slip rate of the Conway Segment of the Hope Fault at Greenburn Stream, South Island, New Zealand. Ann. Geophys. Italy 46, 1119–1140.

Langridge, R., Duncan, R., Almond, P., 2007. Indicators of recent paleoseismic activity along the western Hope Fault GNS Science Consultancy Report 2006/151 (99 pp. + appendices).

Langridge, R.M., Almond, P.C., Duncan, R.P., 2013. Timing of late Holocene paleoearthquakes on the Hurunui segment of the Hope fault: implications for plate boundary strain release through South Island, New Zealand. Geol. Soc. Am. Bull. 125, 756–775.

Langridge, R.M., Ries, W.F., Farrier, T., Barth, N.C., Khajavi, N., De Pascale, G.D., 2014. Developing sub 5-m LiDAR DEMs for forested sections of the Alpine and Hope faults, South Island, New Zealand: implications for structural interpretations. J. Struct. Geol. 64, 53–66.

Lensen, G.J., 1962. Sheet 16-Kaikoura. Geological Map of New Zealand 1:250000, Wellington, New Zealand, Department of Scientific and Industrial Research.

Li, Y.-G., Vidale, J.E., Day, S.M., Oglesby, D.D., Cochran, E., 2003. Postseismic fault healing on the rupture zone of the 1999 M 7.1 Hector Mine, California, Earthquake. Bull. Seismol. Soc. Am. 93, 854–869.

Li, Z., Bruhn, R.L., Pavlis, T.L., Vorkink, M., Zeng, Z., 2010. Origin of sackung uphill-facing scarps in the Saint Elias orogen, Alaska: LIDAR data visualization and stress modeling. Bull. Geol. Soc. Am. 122, 1585–1589.

Lienkaemper, J.J., 2001. 1857 slip on the San Andreas fault Southeast of Cholame, California. Bull. Seismol. Soc. Am. 91, 1659–1672.

Lin, A., Kikuchi, M., Fu, B., 2003. Rupture segmentation and process of the 2001 Mw 7.8 Central Kunlun, China, Earthquake. Bull. Seismol. Soc. Am. 93, 2477–2492.

Lin, A., Ren, Z., Jia, D., Wu, X., 2009. Co-seismic thrusting rupture and slip distribution produced by the 2008 Mw 7.9 Wenchuan earthquake, China. Tectonophysics 471, 203–215.

Lin, A., Rao, G., Yan, B., 2012. Field evidence of rupture of the Qingchuan Fault during the 2008 Mw7.9 Wenchuan earthquake, northeastern segment of the Longmen Shan Thrust Belt, China. Tectonophysics 522–523, 243–252.

Little, T.A., 1996. Faulting-related displacement gradients and strain adjacent to the Awatere strike-slip fault in New Zealand. J. Struct. Geol. 18, 321–340.

Little, T.A., Jones, A., 1998. Seven million years of strike-slip and related off-fault deformation, northeastern Marlborough fault system, South Island, New Zealand. Tectonics 17, 285–302.

Liu, L., Zoback, M.D., 1992. The effect of topography on the state of stress in the crust: application to the site of the Cajon Pass Scientific Drilling Project. J. Geophys. Res. Solid Earth 97, 5095–5108.

Lunina, O.V., Gladkov, A.S., Novikov, I.S., Agatova, A.R., Vysotskii, E.M., Emanov, A.A., 2008. Geometry of the fault zone of the 2003 Ms = 7.5 Chuya earthquake and associated stress fields, Gorny Altai. Tectonophysics 453, 276–294.

Martel, S.J., Pollard, D.D., Segall, P., 1988. Development of simple strike-slip fault zones, Mount Abbot quadrangle, Sierra Nevada, California. Geol. Soc. Am. Bull. 100, 1451–1465.

McCalpin, J.P., 2003. Criteria for determining the seismic significance of sackungen and other scarplike landforms in mountainous regions. In: Hart, E.W. (Ed.), Ridge-Top Spreading in California: California Geological Survey, Open-File Report, 1CD-ROM.

McMorran, T.J., 1991. The Hope Fault at Hossack Station east of Hanmer Basin, North Canterbury, Geological Sciences. University of Canterbury, Christchurch, p. 93.

McTigue, D.F., Mei, C.C., 1981. Gravity-induced stresses near topography of small slope. J. Geophys. Res. 86, 9268–9278.

McTigue, D.F., Stein, R.S., 1984. Topographic amplification of tectonic displacement: implications for geodetic measurement of strain changes. J. Geophys. Res. 89, 1123–1131.

Murata, A., Takemura, K., Miyata, T., Lin, A., 2001. Quaternary vertical offset and average slip rate of the Nojima Fault on Awaji Island, Japan. Island Arc 10, 360–367.

Nathan, S., Rattenbury, M.R., Suggate, R.P., 2002. Geology of the Greymouth area: scale 1:250,000. Lower Hutt: Institute of Geological & Nuclear Sciences. Institute of Geological & Nuclear Sciences 1:250,000 geological map 12. 58 p. + 1 folded map + 65 p.

Nicol, A., Van Dissen, R., 2002. Up-dip partitioning of displacement components on the oblique-slip Clarence Fault, New Zealand. J. Struct. Geol. 24, 1521–1535.

Nicol, A., Wise, D.U., 1992. Paleostress adjacent to the Alpine Fault of New Zealand: fault, vein, and styolite data from the Doctors Dome area. J. Geophys. Res. 97, 17,685–617,692.

Nicol, A., VanDissen, R., Vella, P., Alloway, B., Melhuish, A., 2002. Growth of contractional structures during the last 10 m.y. at the southern end of the emergent Hikurangi forearc basin, New Zealand. N. Z. J. Geol. Geophys. 45, 365–385.

Nissen, E., Krishnan, A.K., Arrowsmith, J.R., Saripalli, S., 2012. Three-dimensional surface displacements and rotations from differencing pre-and post-earthquake LiDAR point clouds. Geophys. Res. Lett. 39.

Norris, R.J., Cooper, A.F., 1995. Origin of small-scale segmentation and transpressional thrusting along the Alpine fault, New Zealand. Geol. Soc. Am. Bull. 107, 231–240.

Norris, R.J., Cooper, A.F., 1997. Erosional control on the structural evolution of a transpressional thrust complex on the Alpine Fault, New Zealand. J. Struct. Geol. 19, 1323–1342.

Norris, R.J., Cooper, A.F., 2001. Late Quaternary slip rates and slip partitioning on the Alpine Fault, New Zealand. J. Struct. Geol. 23, 507–520.

Oglesby, D.D., 2005. The dynamics of strike-slip step-overs with linking dip-slip faults. Bull. Seismol. Soc. Am. 95, 1604–1622.

Oskin, M.E., Arrowsmith, J.R., Corona, A.H., Elliott, A.J., Fletcher, J.M., Fielding, E.J., Gold, P. O., Garcia, J.J.G., Hudnut, K.W., Liu-Zeng, J., Teran, O.J., 2012. Near-field deformation from the El Mayor–Cucapah Earthquake revealed by differential LIDAR. Science 335, 702–705.

Petersen, M.D., Wesnousky, S.G., 1994. Fault slip rates and earthquake histories for active faults in southern California. Bull. Seismol. Soc. Am. 84, 1608–1649.

Petersen, M.D., Dawson, T.E., Chen, R., Cao, T., Wills, C.J., Schwartz, D.P., Frankel, A.D., 2011. Fault displacement hazard for strike-slip faults. Bull. Seismol. Soc. Am. 101, 805–825.

Pettinga, J.R., Wise, D.U., 1994. Paleostress adjacent to the Alpine Fault: broader implications from fault analysis near Nelson, South Island, New Zealand. J. Geophys. Res. 99, 2727–2736.

Pettinga, J.R., Yetton, M.D., Van Dissen, R.J., Downes, G., 2001. Earthquake source identification and characterisation for the Canterbury region, South Island, New Zealand. Bull. N. Z. Soc. Earthq. Eng. 34, 282–317.

Pucci, S., De Martini, P.M., Pantosti, D., 2008. Preliminary slip rate estimates for the Düzce segment of the North Anatolian Fault Zone from offset geomorphic markers. Geomorphology 97, 538–554.

Quigley, M., Litchfield, N., Stahl, T., Noble, D., Jongens, R., Klahn, A., Cox, S., 2010. Surface rupture of the Greendale fault during the Darfield (Canterbury) earthquake, New Zealand: initial findings. Bull. N. Z. Soc. Earthq. Eng. 43 (4), 236.

Quigley, M., Van Dissen, R., Litchfield, N., Villamor, P., Duffy, B., Barrell, D., Furlong, K., Stahl, T., Bilderback, E., Noble, D., 2012. Surface rupture during the 2010 Mw 7.1 Darfield (Canterbury) earthquake: implications for fault rupture dynamics and seismic-hazard analysis. Geology 40, 55–58.

Rattenbury, M.S., Townsend, D., Johnston, M.R., 2006. Geology of the Kaikoura area: scale 1:250,000 geological map. Lower Hutt: GNS Science. Institute of Geological & Nuclear Sciences 1:250,000 geological map 13. 70 p. + 1 folded map

Richard, P., 1991. Experiments on faulting in a two-layer cover sequence overlying a reactivated basement fault with oblique-slip. J. Struct. Geol. 13, 459–469.

Richard, P., Mocquet, B., Cobbold, P.R., 1991. Experiments on simultaneous faulting and folding above a basement wrench fault. Tectonophysics 188, 133–141.

Richard, P.D., Naylor, M.A., Koopman, A., 1995. Experimental models of strike-slip tectonics. Pet. Geosci. 1, 71–80.

Riedel, W., 1929. Zur mechanik geologischer Brucherscheinungen. Centralbl. Mineral. Geol. u. Pal, 1929B, pp. 354–368.

Rockwell, T.K., Ben-Zion, Y., 2007. High localization of primary slip zones in large earthquakes from paleoseismic trenches: observations and implications for earthquake physics. J. Geophys. Res. 112.

Sagy, A., Brodsky, E.E., Axen, G.J., 2007. Evolution of fault-surface roughness with slip. Geology 35, 283–286.

Savage, W.Z., Swolfs, H.S., 1986. Tectonic and gravitational stress in long symmetric ridges and valleys. J. Geophys. Res. 91, 3677–3685.

Savage, W.Z., Swolfs, H.S., Powers, P.S., 1985. Gravitational stresses in long symmetric ridges and valleys. Int. J. Rock Mech. Min. Sci. Geomech. Abstr. 22, 291–302.

Scholz, C.H., 1977. Transform fault systems of California and New Zealand: similarities in their tectonic and seismic styles. J. Geol. Soc. 133, 215–228.

Scholz, C.H., Ando, R., Shaw, B.E., 2010. The mechanics of first order splay faulting: the strike-slip case. J. Struct. Geol. 32, 118–126.

Schulz, S.E., Evans, J.P., 2000. Mesoscopic structure of the Punchbowl Fault, Southern California and the geologic and geophysical structure of active strike-slip faults. J. Struct. Geol. 22, 913–930.

Schwartz, D.P., Haeussler, P.J., Seitz, G.G., Dawson, T.E., 2012. Why the 2002 Denali fault rupture propagated onto the Totschunda fault: implications for fault branching and seismic hazards. J. Geophys. Res. Solid Earth 117, B11304.

Shipton, Z.K., Cowie, P.A., 2001. Damage zone and slip-surface evolution over μm to km scales in high-porosity Navajo sandstone, Utah. J. Struct. Geol. 23, 1825–1844.

Shipton, Z.K., Cowie, P.A., 2003. A conceptual model for the origin of fault damage zone structures in high-porosity sandstone. J. Struct. Geol. 25, 333–344.

Sibson, R., Ghisetti, F., Ristau, J., 2011. Stress control of an evolving strike-slip fault system during the 2010–2011 Canterbury, New Zealand, earthquake sequence. Seismol. Res. Lett. 82, 824–832.

Sieh, K.E., Jahns, R.H., 1984. Holocene activity of the San Andreas fault at Wallace Creek, California. Geol. Soc. Am. Bull. 95, 883–896.

Sieh, K., Jones, L., Hauksson, E., Hudnut, K., Eberhart-Phillips, D., Heaton, T., Hough, S., Hutton, K., Kanamori, H., Lilje, A., Lindvall, S., McGill, S.F., Mori, J., Rubin, C., Spotila, J.A., Stock, J., Thio, H.K., Treiman, J., Wernicke, B., Zachariasen, J., 1993. Near-field investigations of the Landers earthquake sequence, April to July 1992. Science 260, 171–176.

Stirling, M.W., Wesnousky, S.G., Shimazaki, K., 1996. Fault trace complexity, cumulative slip, and the shape of the magnitude–frequency distribution for strike-slip faults: a global survey. Geophys. J. Int. 124, 833–868.

Stirling, M., Rhoades, D., Berryman, K., 2002. Comparison of earthquake scaling relations derived from data of the instrumental and preinstrumental era. Bull. Seismol. Soc. Am. 92, 812–830.

Stirling, M., Gerstenberger, M., Litchfield, N., McVerry, G., Smith, W., Pettinga, J., Barnes, P., 2008. Seismic hazard of the Canterbury Region, New Zealand: new earthquake source model and methodology. Bull. N. Z. Soc. Earthq. Eng. 41, 51–67.

Sylvester, A.G., 1988. Strike-slip faults. Geol. Soc. Am. Bull. 100, 1666–1703.

Tchalenko, J.S., 1970. Similarities between shear zones of different magnitudes. Geol. Soc. Am. Bull. 81, 1625–1640.

Please cite this article as: Khajavi, N., et al., Influence of topography and basement depth on surface rupture morphology revealed from LiDAR and field mapping, Hope Fault, New Zealand, Tectonophysics (2014), http://dx.doi.org/10.1016/j.tecto.2014.05.032

Tchalenko, J.S., Ambraseys, N.N., 1970. Structural analysis of the Dasht-e Bayaz (Iran) earthquake fractures. Geol. Soc. Am. Bull. 81, 41–60.
Treiman, J.A., Kendrick, K.J., Bryant, W.A., Rockwell, T.K., McGill, S.F., 2002. Primary surface rupture associated with the Mw 7.1 16 October 1999 Hector Mine Earthquake, San Bernardino County, California. Bull. Seismol. Soc. Am. 92, 1171–1191.
Van Dissen, R., 1989. Late Quaternary faulting in the Kaikoura region, southeastern Marlborough, New Zealand. Unpublished MS thesis, Oregon State University, USA, 72p.
Van Dissen, R., Yeats, R.S., 1991. Hope Fault, Jordan Thrust, and uplift of the Seaward Kaikoura Range, New Zealand. Geology 19, 393–396.
Van Dissen, R., Barrell, D., Litchfield, N., Villamor, P., Quigley, M., King, A., Mote, T., 2011. Surface Rupture Displacement on the Greendale Fault during the Mw 7.1 Darfield (Canterbury) Earthquake, New Zealand, and its Impact on Man-Made Structures.
Van Dissen, R., Hornblow, S., Quigley, M., Litchfield, N., Villamor, P., Nicol, A., Barrell, D.J.A., Sasnett, P., Newton, K., 2013. Towards the development of design curves for characterising distributed strike-slip surface fault rupture displacement: an example from the 4 September, 2010, Greendale Fault rupture, NZ. In: Chin, C.Y. (Ed.), NZGS Geotechnical Symposium. Queenstown Proc., 19.
Villamor, P., Litchfield, N., Barrell, D., Van Dissen, R., Hornblow, S., Quigley, M., Levick, S., Ries, W., Duffy, B., Begg, J., Townsend, D., Stahl, T., Bilderback, E., Noble, D., Furlong, K., Grant, H., 2012. Map of the 2010 Greendale Fault surface rupture, Canterbury, New Zealand: application to land use planning. N. Z. J. Geol. Geophys. 55, 223–230.
Wallace, L.M., Beavan, J., McCaffrey, R., Berryman, K., Denys, P., 2007. Balancing the plate motion budget in the South Island, New Zealand using GPS, geological and seismological data. Geophys. J. Int. 168, 332–352.
Wallace, L.M., Barnes, P., Beavan, J., Van Dissen, R., Litchfield, N., Mountjoy, J., Langridge, R., Lamarche, G., Pondard, N., 2012. The kinematics of a transition from subduction to strike-slip: an example from the central New Zealand plate boundary. J. Geophys. Res. Solid Earth 117.
Ward, S.J., 2000. The Physical, Chemical and Mineralogical Properties of a Fault Zone, Geological Sciences. University of Canterbury, Christchurch, p. 169.
Warren, G., 1967. Sheet 17- Hokitika. Geological Map of New Zealand 1: 250000, Wellington, New Zealand, Department of Scientific and Industrial Research.
Wells, D.L., Coppersmith, K.J., 1994. New empirical relationships among magnitude, rupture length, rupture width, rupture area, and surface displacement. Bull. Seismol. Soc. Am. 84, 974–1002.
Wesnousky, S.G., 1988. Seismological and structural evolution of strike-slip faults. Nature 335, 340–343.
Williams, P.L., Magistrale, H.W., 1989. Slip along the Superstition Hills fault associated with the 24 November 1987 Superstition Hills, California, earthquake. Bull. Seismol. Soc. Am. 79, 390–410.
Wood, R.A., Pettinga, J.R., Bannister, S., Lamarche, G., McMorran, T.J., 1994. Structure of the Hanmer strike-slip basin, Hope Fault, New Zealand. Geol. Soc. Am. Bull. 106, 1459–1473.
Woodcock, N.H., Fischer, M., 1986. Strike-slip duplexes. J. Struct. Geol. 8, 725–735.
Yang, J.S., 1991. The Kakapo Fault – a major active dextral fault in the central North Canterbury – Buller regions of New Zealand. N. Z. J. Geol. Geophys. 34, 137–143.
Yeats, R.S., Berryman, K.R., 1987. South Island, New Zealand, and Transverse Ranges, California: a seismotectonic comparison (USA). Tectonics 6, 363–376.
Zachariasen, J., Prentice, C.S., 2008. Detailed mapping of the Northern San Andreas Fault using LiDAR imagery. Final Technical Report. U.S. Geological Survey (47 pp.).
Zachariasen, J., Berryman, K., Langridge, R., Prentice, C., Rymer, M., Stirling, M., Villamor, P., 2006. Timing of late Holocene surface rupture of the Wairau Fault, Marlborough, New Zealand. N. Z. J. Geol. Geophys. 49, 159–174.
Zhou, Q., Xu, X., Yu, G., Chen, X., He, H., Yin, G., 2010. Width distribution of the surface ruptures associated with the Wenchuan earthquake: implication for the setback zone of the seismogenic faults in postquake reconstruction. Bull. Seismol. Soc. Am. 100, 2660–2668.
Zischinsky, U., 1966. On the deformation of high slopes. Proceedings of the First Congress of the International Society of Rock Mechanics, Lisbon, Portugal, pp. 179–185.
Zischinsky, U., 1969. Über Sackungen. Rock Mech. 1, 30–52.

Please cite this article as: Khajavi, N., et al., Influence of topography and basement depth on surface rupture morphology revealed from LiDAR and field mapping, Hope Fault, New Zealand, Tectonophysics (2014), http://dx.doi.org/10.1016/j.tecto.2014.05.032